Experimental pathways of clay formation and kinetics of basalt alteration

in poor drainage systems: Implications for weathering

Piyush Sriwastava[1,2], Vijay Kumar Saini[1,3], George Mathew[1]*, Anil D. Shukla[4]

[1]Department of Earth Sciences, Indian Institute of Technology Bombay, Mumbai, Maharashtra 400076, India
[2]Museum of Natural History, University of Oxford, Parks Road, Oxford, OX1 3PW, UK
[3]Helmholtz-Zentrum Dresden-Rossendorf e. V.- Institute of Resource Ecology, Bautzner Landstraße 400, 01328 Dresden, Germany
[4]Physical Research Laboratory, Ahmedabad, Gujarat 380059, India

Abstract

Basalt being the most dominant rock on the earth's crust, contributes significantly to the global elemental cycle through weathering. In recent years, the potential of basalt weathering has been continuously scrutinized as a carbon dioxide removal (CDR) strategy. An accurate estimation of such large-scale processes requires a deeper insight into the mechanism controlling the basalt glass dissolution under field conditions. This contribution assesses the chemical evolution of fluid interacting with basalt glass in poorly drained regimes. Experiments showed a drop in kinetics of alteration ($r_0 = 1.7 \times 10^{-9}$ mol.m^{-2}. s^{-1}) by two orders of magnitude in 24 days and emphasizes the onset of secondary mineral formation within 20 hr of the start of dissolution. At first, Mg starts fractionating from the solution due to brucite oversaturation and reaches undersaturation after 60th hour due to onset of other Mg-bearing minerals. From the 54th hour, montmorillonite remains oversaturated until Mg is entirely consumed by precipitation at the 164th hour. SEM-EDS investigation shows the presence of two major morphologies of secondary products: (a) honeycomb shape (smectite), with high Mg (>3 wt%) and octahedral composition similar [(Si/Al+Fe+Mg) and Al/Si] to smectite, (b) aggregate of ellipsoid and/or equant granular phases. Compositionally, elliptical and granular aggregates show affinity towards low Mg and high Fe variety of smectite amorphous precursor. The absence of pure brucite grains indicates epitaxial growth of Mg-rich, honeycomb-shaped phyllosilicate
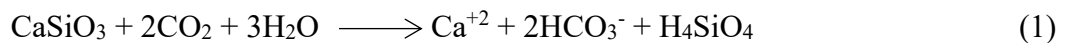
29 precursor on the brucite template due to well-reported structural similarity between the brucite

30 layer and 2:1 phyllosilicate octahedral sheet. Elliptical and equant-shaped grains with or

31 without compositional similarity with smectite phases have high Fe and low Mg, indicating

32 their formation under a low Mg concentration stage in solution. Precipitation of the secondary

33 phases at various stages of reaction progress affects the total reaction affinity in a closed

34 system. Coupled dissolution and precipitation at the fluid-rock interface are responsible for

35 lowering the kinetics of dissolution reactions in a closed system, previously explaining the slow

36 kinetics of natural weathering regimes. The damped kinetics of dissolution and cations

37 fractionation in secondary products within a few hours of onset of dissolution reaction can

38 result in an overestimation (ten times) of CDR potential estimation by enhanced rock

39 weathering (ERW) if calculations do not involve the nature of closed system evolution during

40 basalt glass alteration.

41

44
45 *Corresponding Author: gmathew@iitb.ac.in

1. Introduction:

Silicate weathering, viz., disintegration and decomposition of rock, drives the element cycle on earth surface (Frings and Buss, 2019). Ions released during chemical weathering have two crucial fates: (1) carried away by river from catchment or (2) captured in neoformed secondary minerals, e.g., clays, carbonates or metal (oxy)hydroxide (Velde and Meunier, 2008), that are vital for organisms nutrient turnover (Fang et al., 2023). Rivers in basaltic terrain have shown the highest cationic flux due to highly reactive constituents in basalt such as amorphous interstitial glass, pyroxene and olivine (Eggleton et al., 1987; Nesbitt and Wilson, 1992; Hermanska et al., 2023) resulting $30 - 35\%$ of global CO_2 fixation in the form of bicarbonates of cations, that later lead to carbonate precipitation (Dessert et al., 2003). The dominant pathway of carbon dioxide removal (CDR) by weathering of basalt can be expressed by chemical reaction:

$$CaSiO_3 + 2CO_2 + 3H_2O \longrightarrow Ca^{+2} + 2HCO_3^- + H_4SiO_4 \tag{1}$$

Basalt weathering has not only significant control over the long-term CO_2 content in atmosphere but also on global cycle of elements and chemistry of earth's critical zone (Kump et al., 2000; Dessert et al., 2001; Stefansson and Gislason, 2001). The rate of CO_2 fixation can be increased by enhanced kinetics of basalt dissolution (Schuiling and Krijgsman, 2006), which is achieved by addition of finely crushed basalt (Goll et al., 2021; Rinder and Hagke, 2021; Vienne et al., 2022). Beerling et al. (2020), Strefeler et al. (2018) and Taylor et al. (2016) have demonstrated that enhanced weathering of basaltic rock can be adopted as potential CO_2 removal strategies as it can capture 10.5 ± 3.8 t CO_2 ha^{-1} (Beerling et al., 2024) if applied in croplands which also enhances the food security and crop productivity. According to reaction (1), the large-scale estimation of CDR potential will directly depend on bivalent cations supply rate and residence time, which depend on the kinetics of basalt dissolution and proximity of the system to equilibrium or precipitation conditions, respectively. Most large-scale

calculations are based on basalt dissolution models under open systems, which are far from equilibrium. Natural weathering in near-surface environments is dominated by poor drainage systems, where fluid leads to coupled dissolution and precipitation at the fluid-rock interface.

Numerous studies have been done to understand initial basalt dissolution kinetics over a wide range of temperatures and pH in an open system (e.g. Gislason and Eugster, 1987a; Guy and Schott, 1989; Crovisier et al., 1988a, 1988b, 1990, 1992, 2003; Daux et al., 1994, 1997). Oelker and Gislason (2001) and Heřmanská et al. (2023) have proposed an empirical formula to calculate the steady state rate (r) of basalt glass dissolution in an open system, far from the equilibrium. However, basalt dissolution in a closed system remains less probed. Daux et al. (1997) studied basalt dissolution kinetics evolution using multiple open systems with high flow rates resulting far from equilibrium systems and low flow rates resulting near equilibrium systems analogous to closed systems. Following transition state theory, the steady-state rate of each reaction setup strongly correlated with reactions Gibbs free energy (ΔG_r). Techer et al. (2001) investigated the general dissolution model based on TST to explain the basalt dissolution kinetics in a closed system approaching equilibrium. However, the relationship between kinetic evolution and total chemical affinity remains unexplained. Although closed systems kinetics evolution has been understood for minerals like alkali feldspar with coupled dissolution-precipitation during alteration reaction in a closed system (Alekseyev et al., 1997; Zhu and Lu, 2009; Zhu et al., 2010), such an approach requires a mechanistic understanding for basaltic glass.

According to current understanding, basalt interaction with water starts with H_2O diffusion and hydration of a silicate network followed by a metal proton exchange reaction, resulting in a hydrated glass layer (Bourcier et al., 1992; Angeli et al., 2006). Initially, the diffusion rate is higher than the hydrolysis rate; eventually, with increasing thickness of the hydrated glass layer, diffusion rates slow down to the hydrolysis rate, and the dissolution

96 reaction becomes congruent (Gislason and Eugster, 1987; Crovisier., 1992). Hydrolysis at

97 higher temperatures occurs partially, resulting in a porous surface layer facilitating diffusion

98 (Berger et al., 1987, 1988, 1994), while hydrolysis is total at low temperatures. Neeway et al.

99 (2016) have proposed an alkali interdiffusion model based on Fick's law for quantitatively

100 constraining the diffusion parameters. Bouakkaz et al. (2016) studied glass (SON68)

101 dissolution in an open system (flow-through reactor) using ^{29}Si doped fluid and showed that

102 both diffusion and surface alteration reactions govern glass dissolution. Bouakkaz and others

103 reported that the hydrated glass layer is Mg-poor. Secondary products are Mg-rich silicates,

104 indicating a unique role of Mg during glass alteration reaction, as envisaged in the present

105 work. Since basalt dissolution kinetics is controlled by surface reactions (Berner, 1978; Murphy

106 et al., 1989), many researchers have attempted to establish a general relation between reaction

107 rates and chemical affinity under Transition State Theory (TST), considering the desorption of

108 different surface complexes as a rate-defining step. Grambow (1985) considered desorption of

109 purely siliceous surface complex as a rate-defining step and proposed first-order rate law,

110 which is a function of proton activity in solution [H$^+$] and activity of orthosilicic acid [H$_4$SiO$_4$].

111 Berger et al. (1994) considered =SiOH as a precursor species, and the basalt dissolution rate

112 was a function of 0.33 power of Q/K, where Q is precursor species activity, and K is amorphous

113 silica hydrolysis reaction's solubility constant. The power value (0.33) in this rate calculation

114 equation depends on the silica retention amount in the alteration gel, which varies with

115 temperature. Daux et al. (1997) studied the dissolution kinetics of basalt at 90°C and considered

116 hydrolysis of a hydrated glass layer with composition Si, Al, Fe and H$_2$O as a determining step.

117 Although numerous attempts have been made to unveil the mechanism of basalt dissolution

118 and establish kinetics relations in an open system, the fate of ions released in a closed system

119 needs investigation from the perspective of kinetics evolution, the effect of equilibrium on

120 kinetics and pathways of secondary mineral formation.

121 Hence, the current study has investigated the pathways of basalt glass alteration in

122 alkaline conditions under a closed system as water bodies in basaltic terrain become alkaline

123 (Gislason et al., 1996; Reimers et al., 1996; Dessert et al., 2001; Pokrovsky et al., 2005). We

124 have used basalt glass rather than a crystalline rock for two reasons: (1) each crystallised basalt

125 contains variable amounts of interstitial glass and crystalline components. The dissolution rate

126 of glass being faster than crystalline controls the pathways of precipitation reaction, (2) to

127 bridge the knowledge gap of glass dissolution mechanism and kinetics, which is crucial for

128 reaction path modelling of normal basalt in which the crystalline components, e.g., pyroxene

129 and plagioclase have been well understood.

130 In the present contribution, we have evaluated the following two problems associated

131 with basalt glass alteration in closed-system that hold importance from the perspective of a new

132 strategy of CDR using ERW of basalt glass: 1) Evolution of alteration kinetics, ΔG_r and

133 pathways of secondary mineral formation in a closed alkaline system and 2) The disparity

134 between dissolution rate estimation and total reaction affinity in a closed system following

135 TST, explained by coupled dissolution and precipitation reactions. We have also estimated the

136 impact of poor drainage conditions on CDR potential.

137

138 **2.   Material and Methods:**

139 **2.1. Sample preparation**

140 The basalt glass used in this study is a natural glass collected from Hawaii Island. It was

141 ground using agate mortar to increase the reactive surface area. The ground sample was sieved

142 to obtain 36–56 μm and less than 36 μm size fraction. The 36 –56 μm fraction was cleaned

143 with ultrasonic bath to remove the ultra-fine particles. First, cleaning was done for 10 minutes

144 in deionised water, followed by acetone. Five to six cleaning cycles with water and acetone

145 were sufficient to remove all fine particles from 36–56 μm fraction. Subsequently, the sample

146 was dried overnight at 60°C.

147 **2.2 Experiment Setup**

148 The experiment was performed in a custom-made setup (Fig.1). A closed four-necked

149 round bottom flask was equipped with a temperature sensor probe connected to the solution

150 and a PID controller. The flask was kept on a heating mantle, having a rounded opening with

151 woven fabric in the surroundings, to heat homogeneously. The heater system and PID controller

152 were synced to maintain the system's temperature within the ±1°C range. A mechanical stirrer

153 was employed in the reaction setup to keep the reacting grains of basalt glass in suspension

154 throughout the reaction. There was a retractable outlet system and a PTFE syringe of 5 ml

155 connected with a flexible teflon pipe. 1.25 ml of the solution was piped out at regular intervals.

156 Each sample was filtered using a 0.2 μm cellulose filter before analysis. After each sampling

157 step, outlet systems were cleaned and dried to avoid contamination from the previous sample.

158 The reaction was kept at 90°C with a 1:500 rock-water ratio (0.6 g rock in 300 ml solution).

159 Graham condenser was attached to flask with a sealed top to condense vapour and avoid

160 increased pressure in the reaction chamber. The pH of the reacting solution was measured at

161 regular intervals by inserting a pH-measuring electrode connected to a digital meter. pH

162 measurement was calibrated for 90°C. The starting fluid was slightly alkaline, with a pH of

163 8.3. Reacting alkaline fluid was prepared using NaOH (Merck) in milli-Q water.

164 **2.3 Analytical Methods**

165 The surface area of the grains was measured using Brunauer-Emmett-Teller Method

166 (BET). The crystalline and amorphous nature of basalt glass and the secondary clay products

167 was evaluated with X-ray diffraction (XRD). The crystal chemistry of raw glass and the

168 secondary product was studied using Fourier transform infrared (FTIR) spectroscopy. Textural,

169 morphological and analytical study of sub-micron-sized secondary product was performed

170 under scanning electron microscopy (SEM) with energy dispersive X-ray spectroscopy (EDS).

171 The chemical composition of fluid and basalt glass was determined using inductive coupled

172 plasma atomic emission spectroscopy (ICP-AES) and mass spectroscopy (MS).

173   The specific surface area of the samples was measured on Quantachrome Nova 2000e at

174 the University of Vienna, Austria, using the six-point Brunauer-Emmett-Teller (BET) method.

175 The sample with grain size 36–56μm has a surface area of 4.51 ± 0.01 m^{2}g$^{-1,}$ while sample with

176 grain size <36 μm has a surface area of 6.38 ± 0.33 m^2.g^{-1}. The X-ray diffraction (XRD) analysis

177 was performed at the Department of Earth Sciences, Indian Institute of Technology (IIT)

178 Bombay, with Empyrean Panalytical XRD. X-ray was generated with a Cu target. The X-ray

179 spectra were collected with 0.01° step increment and a count time of 58.395 s per step using

180 Cu Kα radiation transmitted through 0.04 rad soller slit opening and 1.52 mm anti-scatter slit.

181 The diffracted beam was detected using a PIXcel^{3D} detector.

182   The Fourier transform infrared (FTIR) measurements were performed on Thermo Nicolet

183 6700 and Bruker Vertex 80 FTIR systems at the Department of Earth Sciences and

184 Sophisticated Analytical Instrument Facility (SAIF), IIT Bombay. Sample powder was mixed

185 with KBr (2 mg of sample and 200 mg of KBr), and a pressed disc was prepared. Spectra were

186 collected in the range of 400–4000 cm^{-1} with a resolution of 2 cm^{-1}. The decomposition of OH-

187 stretching bands into component peaks was done using fityk 1.3.1 software (Wojdyr, 2010). It

188 uses the Levenberg-Marquardt method for curve fitting. Curve fitting parameters were

189 accepted based on a weighted sum of squared residuals (WSSR) parameters and agreement

190 between calculated and experimental profiles.

191   The solution's Na, K, Ca, Mg, Al, and Si concentrations were measured using Spectro

192 Arcos Inductively coupled plasma atomic emission spectroscopy (ICP-AES) at SAIF, IIT

193 Bombay. The instrument was calibrated for 0.1 ppm to 100 ppm using a multielement standard

194 prepared by serial dilution. The precision and accuracy of the analysis were better than 5%,

195 and the blanks were negligible. Accuracy and precision were continuously monitored using

196 standard as unknown. The detection limit of the instrument was 0.01 ppm. Lithium

197 concentration in the basalt glass and reacting fluid was measured using ThermoIcap quadrupole

198 Inductively coupled plasma mass spectroscopy (ICP-MS) at the Department of Earth Sciences,

199 IIT Bombay. BHVO-2 (Hawaiian basalt), RGM-2 (Rhyolite from Glass Mountain), STM-2

200 (Syenite), SBC-1 (Brush Creek shale), and SCO-2 (Cody shale) rock standards were used for

201 calibration and accuracy during the Li concentration measurement of basalt glass. Rock

202 standards and basalt glass were digested using microwave acid digestion technique. Reacting

203 fluid chemical analysis was calibrated using multielement standards of different

204 concentrations, prepared by serial dilution. Precision and accuracy in both analyses were below

205 5%.

206 Imaging of submicron to sub-nano meter sized secondary product of basalt glass

207 alteration reaction was done at Physical Research Laboratory (PRL) India, using a scanning

208 electron microscope (SEM) (model JEOL IT300). Insitu compositional measurement was done

209 under an energy dispersive spectrometer (EDS) attached to SEM. An ion sputtering coater was

210 used to create a conductive carbon layer before imaging to avoid charging in SEM. In situ

211 chemistry of basalt glass grains was measured at the Department of Earth Sciences, IIT

212 Bombay (India), using a Cameca SX-50 electron microprobe analyser (EPMA) with five

213 wavelength dispersive spectrometers. Glass grains were mounted in epoxy stubs and finely

214 polished. Carbon coating was done before analysis under EPMA to avoid charging. Analysis

215 was done using a pointed probe (diameter 2 μm) at an acceleration voltage of 15 kV and a fixed

216 probe current of 20 nA.

217 **2.4 Geochemical Modelling:**

218 PHREEQC computer program (C++ language) was used to perform aqueous

219 geochemical calculations at low temperatures (Parkhurst and Appelo 1999). Speciation and

220   solubility geochemical modelling was done for each reaction step (sample) to calculate product

221   minerals saturation indices (SI). The molar concentration of elements in each sampled solution,

222   fluid temperature, pH, and volume were used as input parameters to calculate the activity of

223   chemical species. The Graham condenser attached to the chamber maintained pressure at 1 atm

224   in the reaction chamber. Hence, the modelling parameter for pressure was set by default as 1

225   atm. The simulated pH was also compared with the experimentally measured pH (see Table S4

226   and Table S5). The activity of chemical species was used to calculate the Gibbs free energy of

227   each reaction step (ΔG_r). The Carbfix and MINTEQ databases were used in the modelling.

228   **2.5 Dissolution rate determination:**

229   The kinetics of dissolution is a measure of rate of mass dissociation from reactant.

230   Element concentration continuously increases during dissolution in a closed system, while an

231   open system results in a mechanical steady state of elements defined by flow rate. The amount

232   of element released in the solution at any stage of the reaction can measure the dissolved mass

233   of basalt glass if the element does not fractionate in any secondary product. Many researchers

234   have considered Li as a tracer element for dissolution studies (Vernaz et al., 2001; Techer et al.,

235   2001; Curti et al., 2006; Gin et al., 2013; Parruzot et al., 2015). Li concentration and changed

236   solution volume were used after fluid removal in the previous sampling step to calculate the

237   mass loss of basalt during dissolution. Normalised mass loss (NML) measures mass loss per

238   unit surface area of reacting basalt. It can be calculated using the following equation:

239

240 $$\text{Normalised Mass Loss (NML)} = (^{n}C_{Li} \times {}^{n}V) / (R_{Li} \times S) \qquad (2)$$

241      $^{n}C_{Li}$ = concentration of Li in fluid at n^{th} hour

242   ^{n}V = volume of fluid at n^{th} hour

243   R_{Li} = concentration of Li in rock

244   S = total surface area ($m^2 g^{-1}$)

245   The alteration rate of basalt glass for each sampling step can be measured using the difference

246   between normalised mass loss in two consecutive steps and the time gap between them. The

247   formula to measure alteration rate in "mole m^{-2} s^{-1}" can be written as follows:

248

249   Alteration rate $r_{[i + (i+1)]/2}$ = [$(NML)^{i+1}$ – $(NML)^{i}$] / [$(t^{i+1}$ - t^{i}) × (molecular mass)   (3)

250

251   **2.6 Gibbs free energy calculation:**

252   In recent years, mineral dissolution kinetics has been investigated using transition state

253   theory. Nagy et al. (1991), Nagy and Lasaga (1992), Lasaga et al. (1994) proposed a model to

254   study kinetics by incorporating "reaction affinity" term in ΔG_r measurement ($A = -\Delta G_r$):

$$r = k^+ \left(\prod_J a_J^{m_J} f(\Delta G_r) \right) \qquad (4)$$

256   r is the mineral dissolution rate, k+ is the rate constant, $\prod_J a_J^{m_J}$ shows the activity product of

257   species in the solution, $f(\Delta G_r)$ is the Gibbs free energy function, which can be expressed as

258   follows (Aagaard and Helgeson, 1982; Nagy et al., 1991; Lasaga et al., 1994):

259      $f(\Delta G_r) = 1 - \exp(n\, \Delta G_r / RT)$ (5)

260   For the current experimental setup, we measured Gibbs free energy of each incremental

261   reaction with dissolution of basalt glass using the following equation:-

262      $Q/K_e = \exp(\Delta G_r / RT)$ (6)

263   Q is the ion activity product, K_e is the solubility product, R is the ideal gas constant, T is the

264   temperature, and ΔG_r is the reaction Gibbs free energy. The final rate equation used was:

265      $R = k^+(1 - Q/K_e)$ (7)

266 Following Paul (1977), basalt glass solubility product (K_e) was calculated by considering glass

267 a mixture of oxide. x_i (molar fraction) and K_i (solubility products) of each oxide are known.

268 Hence, the solubility of glass has been calculated using ideal solid solution relation (Bourcier

269 et al., 1992; Advocat et al., 1997; Leturcq et al., 1999):

270 $$\log K_e = \sum_i x^i \log K^i + \sum_i x^i \log x^i \qquad (8)$$

271 **3. Results:**

272 **3.1 Basalt Glass Characterisation**

273 The Hawaiian basalt glass powder X-ray diffraction (XRD) pattern has no discernible

274 peaks, indicating the absence of crystalline phases. XRD spectra showed a broad low-intensity

275 hump in the range of 25–30° 2θ (Fig. 2A), characteristic of amorphous material (Dehouck et

276 al., 2014; Rowe and Brewer, 2018;). The specific surface area (SSA) of basalt glass, in size

277 range <36 μm, is 6.38 ± 0.33 m^2/g; comparatively, 36-56 μm size fraction has a lower, 4.51 ±

278 0.01 m^2/g, specific surface area (measured using the BET method) (Table1). SEM images of

279 basalt grains show several characteristic morphological features of amorphous glass, e.g.,

280 conchoidal fractures, blocky irregular surfaces, etc. (Loocks et al., 2010). Under an electron

281 microscope, glass grains appear micro-pores or pits-free. BSE images (Fig. 2C) of glass

282 fragments under EPMA show homogeneous grey shades across all grains, suggesting a lack of

283 compositional heterogeneity within and between the grains. The bulk chemistry of basaltic

284 glass measured with ICP-AES shows that almost all element's concentration lies within the 1σ

285 range of 25 grains chemistry measured under EPMA (Table 2). This confirms the

286 compositional homogeneity of basaltic glass fragments and discards the possibility of site-

287 specific variation in the glass dissolution reaction due to chemical heterogeneity of the reacting

288 substrate within a system. The total alkali in glass (K_2O + Na_2O = 2.87 wt%) is less than 5

289 wt%, and SiO_2 (52.50 wt%) lies between 45 and 54 wt%, which is in the range of basalt as per

290   the TAS diagram of rock classification (Bas et al., 1986). FeO (t), MgO, Al_2O_3, TiO_2, and CaO

291   also lies in the range of basalt. Li concentration in the basalt glass is 5.27 ppm (Table 2).

3.2 Evolution of pH and elements in fluid

293   The experiment started with slightly alkaline fluid (pH=8.7) under a closed system.

294   Unlike previous studies in open systems (far from equilibrium), closed systems show a

295   dynamic evolution in the fluid composition (Crovisier, 1987, 1988a, 1988b; Daux, 1997;

296   Techer et al., 2001; Oelker and Gislason, 2001; Gislason and Oelker, 2003; Wolff-Boenisch,

297   2004; Declercq et al., 2013). The pH increases rapidly and reaches a plateau at 9.35-9.40 within

298   48 hours of the reaction. After 284 hours, pH drops to an initial value of ~8.5 and remains

299   almost constant from 300 hours onwards (Table 3). Lithium (Li) concentration in the basalt

300   glass is in trace amount (~5 ppm). As Li is highly mobile, it liberates from reacting solid quickly

301   and does not fractionate to any secondary phase. The concentration of Li in both dissolution

302   experiments shows an overall trend of increase with time (Table 3), reaching a value of 4 ppb

303   in 548 hours.

304   The Fe concentration was below the detection limit of analysis. This experimental setup

305   has oxidation conditions similar to recent earth's surface. Under oxidising conditions, iron

306   attains a ferric state (Fe^{+3}) and goes into solid phases, e.g., iron (oxy) hydroxide, resulting in

307   very low Fe^{+3} (aq) (Fox, 1988). Other than Fe, all major cations present in basalt (Na, K, Ca,

308   Si, Mg and Al) have been measured in reacting fluid to monitor the dissolution reaction and

309   subsequent fluid evolution in both experiments. Na, K increases rapidly compared to Ca, Mg,

310   Al and Si in the first few hours under both experimental setups (Fig. 3). Except for Mg, other

311   cations (Na, K, Ca, Al and Si) reach their local maximum concentration after 54 hours, followed

312   by a sudden decrease within 6 hours (Fig. 3). After 60 hours, cations (Na, K, Ca, Al and Si)

313   concentration in solution continuously increases with different trends. The elemental

314   concentration evolution of Mg behaves differently. Mg reaches a plateau value of ~1.70 ppm

315 at 20 hours and remains almost the same till 54 hours. This is followed by a continuous drop

316 in concentration, which is contemporary to other cations' concentration drop stage until Mg

317 concentration exceeds the detection limit. The time of Mg disappearance from the solution

318 differs in both experiments, 164 hours in <36 μm and 236 hours in 36–56 μm. Cations show a

319 change in the concentration increment behaviour from the Mg loss point in the solution. This

320 concentration evolution pattern is similar in both experimental conditions.

321 **3.3 Secondary products**

322 Pre-experimental characterisation of glass surfaces has been performed in detail.

323 Submicron features have been investigated under an analytical electron microscope (SEM-

324 EDS). SEM imaging of basalt glass surface in both experiments shows secondary products in

325 the form of coating. The morphologies of secondary products can be categorised into two major

326 types: a) honeycomb-like structure grown on the glass surface (Fig. 4 A, C) and b) equant

327 and/or ellipsoid grains accumulated on the surface (Fig. 4 B, D). In both experiment setups,

328 these features are present with varying chemical compositions and assemblages, encompassing

329 the signature of reaction progress associated with their formation (Table 4).

330 In the experiment with <36 μm glass fraction, a secondary product having honeycomb

331 morphology is a dominant phase with a size of up to a few microns (Fig. 4 A). In Fig. 4A, the

332 sporadic presence of small particles with honeycomb structures attached to the large grain

333 surface indicates a smaller fraction of the original basalt glass. Chemically, both features have

334 similar compositions and are slightly modified to the initial basalt glass (Table 4). Cation ratios,

335 Si/(Al+Mg+Fe) and Al/Si, based on 11 oxygen, lie between 1-2 and 0-0.4, respectively,

336 depicting a close chemical affinity towards nontronite or saponite type of 2:1 phyllosilicate

337 (Fig. 4 E) (Cuadros et al., 2013). Other secondary products in this experiment setup are

338 aggregates of phases with ellipsoidal morphology and equant granular morphology (Fig. 4B).

339 Chemically, ellipsoid phases have Si/(Al+Mg+Fe) between 1-2 and Al/Si > 0.4, which can be

340 compositionally categorised as montmorillonite (2:1 phyllosilicate) (Fig. 4E). Ellipsoid phases

341 are Mg depleted and K enriched compared to honeycomb morphology (Table-4). Equant

342 granular phases, co-existing with ellipsoidal morphotypes (Fig. 4B), are smaller in size (<0.5

343 microns) with relatively lower Fe, Mg and Ti with increased anions (oxygen) wt%, suggesting

344 calcium-aluminium hydrous silicates (CAHS). The cation ratios, $2 < Si/(Al+Mg+Fe) < 1$ and

345 Al/Si>1, fall out of the 2:1 phyllosilicate range (Fig. 4E).

346 In the experiment with 36-56 μm glass grains, secondary products having honeycomb

347 morphology are dominant phases grown as glass surface coating. Chemically, these phases are

348 Fe (>17 wt%), Mg (>3 wt%) and Ca (> 9wt%) enriched, with Si/Al+Mg+Fe (between 1-2) and

349 Al/Si (< 0.4) values showing close affinity to nontronite/saponite, 2:1 phyllosilicate (Fig. 4E).

350 Other secondary products are sub-nano-meter phases with equant growth. Based on their

351 morphology, they could be categorised into two major types: (1) Equant aggregate phase and

352 (2) Equant granular phase (Fig. 4D). Although equant aggregate phases show a compositional

353 similarity with nontronite and saponite (Fig. 4E) because Si/(Al+Mg+Fe) lies between 1-2 and

354 Al/Si <0.4, but Mg (<3 %) is lower than honeycomb-shaped phases (Table-4). Equant granular

355 phases are found at glass surfaces as isolated nano to micron-size mounds. They do not show

356 chemical affinity towards any 2:1 phyllosilicate, Si/(Al+Mg+Fe), and Al/Si lies out of the range

357 for phyllosilicate (Fig. 4E). High Fe (average 43 wt.%, n=5), Ti and low Mg, Si are distinct

358 compositional identities of equant granular phases.

359

360 **4. Discussion**

361 **4.1 Dissolution behaviour and kinetics**

362 Dissolution reaction under an open system attains a steady state far from equilibrium,

363 resulting in no precipitation. Hence, mobile cations, e.g. Na and K, were used as a proxy to

364 measure the extent of dissolution in open systems (Daux et al., 1997; Techer et al., 2001).

365 Closed systems reach equilibrium due to a continuous increase in the elemental concentration,

366 resulting in the precipitation of saturated phases and causing the fractionation of elements in

367 the solid against the release in the solution. After an extent of reaction progress, closed systems

368 experience a combination of dissolution and precipitation, requiring a highly mobile element

369 (Li) as a proxy to calculate the dissolution extent, behaviour and kinetics. Although Li is highly

370 mobile, it can substitute Mg in the octahedral clay sites due to similarity in ionic radii (Shannon,

371 1976). Li fractionation in the current experimental condition, calculated based on expression

372 of partition coefficient ($\log D_{Li}$) proposed by Decarreau et al. (2012), is within the error of Li

373 concentration measurement for quadrupole (Q)-ICPMS (see Table S9 and Table S10). Note

374 that this calculation is based on expression proposed for hectorite (Li-Mg clay). The current

375 experimental product's Mg concentration (~4%) is lower, leading to a lower partition

376 coefficient.

377   The Li concentration measured at each step of dissolution reaction gives the extent to

378 which basalt glass was dissolved (using eqn 1). Both size fractions of basalt glass show a

379 similar trend of normalised mass loss variation during the entire extent of dissolution reaction

380 (Fig. 6). Smaller fraction (<36 µm) has higher values of normalised mass loss in comparison

381 to larger fractions (36–56 µm) at any extent of time (Fig. 6), due to larger surface area (Table-

382 1). Starting at 100 hours, normalised mass loss increases rapidly for both the fraction and slows

383 down afterwards. Mass loss evolution with time is exponential (r^2 = 0.74–0.77) (Fig. 6). Basalt

384 glass dissolution rate for a smaller fraction (<36 µm), calculated in the initial days of reaction,

385 is (r_0) 1.7×10^{-9} mole.m^{-2}.s^{-1}, which lowers by 100 times by the end of 24 days to (r) 5.7×10^{-11}

386 mole.m^{-2}.s^{-1}. The initial dissolution rate of a larger fraction is 2.5×10^{-9} mole.m^{-2}.s^{-1}and the final

387 rate (after 24 days) is 6.5×10^{-11} mole.m^{-2}.s^{-1}.

388   In both experimental setups, elemental evolution patterns with time are similar (Fig.

389 3). Elemental ratios (Li/Si, Al/Si, Mg/Si, Ca/Si) in reacting fluid show higher values in the

390   initial 20 hours (Fig. 5) for basalt glass, suggesting a preferential removal of modifier cations

391   in silicate structure due to proton-metal exchange reaction (Ghiara et al., 1993, Gin et al., 2013).

392   Such dissolution behaviour indicates an incongruent nature. The protonation of silicate

393   structure causes an increase in pH (Fig. S3). The ratio of Li/Si in fluid and basalt glass reaches

394   similar values after 20 hours (Fig. 5). It remains almost constant later, indicating the congruent

395   nature of the dissolution reaction afterwards, with minor fluctuations signifying the equilibrium

396   with saturated phases. Other cations (Al, Mg, Ca) ratio with Si in the fluid decreases below the

397   glass values (Fig. 5). It reaches a plateau, indicating preferential incorporation of these cations

398   in the precipitation of secondary phases.

4.2 Secondary product formation mechanism: Implication towards phyllosilicate nucleation

401   Basalt glass dissolution reaction in a closed system has resulted in a continuously

402   evolving fluid chemistry (Fig. 3). Aqueous geochemical modelling of this dynamic system

403   shows the possible mineral phases undergoing supersaturation (see Table S1 for saturation

404   index) at each stage of reaction progress (Fig. 7). Despite the continuous dissolution of glass,

405   Mg concentration in the reacting solution reached a plateau within 20 hours, corresponding

406   with brucite [$Mg(OH)_2$] supersaturation (Fig. 7). Although brucite was an oversaturated phase

407   from the 4th hour onwards, according to thermodynamics, its precipitation started with a lag of

408   14 -16 hours due to nucleation delay associated with lower degree of supersaturation, called

409   induction period (Spanos and Koutsoukos, 1998; Brown, 2011). At 54th hour, a decrease of

410   elemental concentration, e.g. Al, Si, Ca along with Mg in the reacting solution signifies the

411   start of another solid phase, Ca-montmorillonite (smectite), indicating oversaturation (Fig. 7)

412   at this stage of the system. After 6 hours of brucite and smectite coprecipitation, Mg

413   concentration reaches below ~1 ppm, resulting in a brucite undersaturation state at 60th hour,

414   leaving smectite (Ca- montmorillonite) as the only saturated phase afterwards. The sudden

415 disappearance of montmorillonite (smectite) from an oversaturation state at the 160th hour

416 corresponds to Mg concentration below the detection limit (0.01 ppm). Record of element

417 concentration evolution and theoretical estimation of mineral supersaturation suggested two

418 significant stages of smectite precipitation in this system: (1) smectite (2:1 phyllosilicate)

419 coprecipitation with brucite and (2) only smectite precipitation.

420 SEM-EDS study of secondary products shows honeycomb-shaped features in both

421 experimental conditions with high Mg (>3 wt.%). Many researchers have reported the

422 honeycomb-shaped morphology as a characteristic feature of smectite (Keller et al., 1986;

423 Fiore et al., 2000; De La Fuente et al., 2000; Christidis, 2006). Compositionally, the honeycomb

424 structure is closely related to the nontronite and saponite smectite (Fig. 4E). Other secondary

425 products with smectite chemical affinity, e.g., the ellipsoidal and equant aggregate phases, have

426 low Mg and high Fe. None of the secondary phases observed has brucite chemistry (Fig. 4),

427 although fluid composition and thermodynamic modelling have shown a strong signature of

428 precipitation (Figs. 3,7). This suggests either the transformation/incorporation of brucite

429 structure into other stable phases or its dissolution, which should have shown an increased Mg

430 concentration. After the first appearance of brucite in the system, there was no signature of Mg

431 concentration increment, neglecting the dissolution hypothesis for the absence of brucite.

432 Several studies have shown that brucite-like structure is an intermediate stage of smectite

433 formation or transformation (Banfield et al., 1991; Bettison-Varga and Mackinnon, 1997;

434 Meunier et al., 2010; Meng et al., 2018) since brucite has structural similarity with octahedral

435 sheet of clay (Tsipursky and Drits, 1984; Chakoumakos et al., 1997). Hence, brucite constitutes

436 the perfect template for smectite epitaxial growth. Brucite oversaturation before

437 montmorillonite (smectite) saturation (Fig. 7) might facilitate high Mg smectite growth viz.

438 honeycomb shaped in both experimental conditions (Table-4). The smectite oversaturation

439 without brucite (Fig. 7) might indicate the secondary product formation stage with low Mg,

440 e.g. ellipsoid phase and equant aggregate (Fig. 4E). Powder x-ray diffractogram collected at

441 the end of the experiment shows an absence of diffraction peaks (Fig. S1), suggesting

442 secondary products as amorphous precursors for crystalline mineral varieties. The FTIR spectra

443 of both the experimental products in the stretching region of OH vibration show metal-OH

444 bonds overlayed by glass spectra (Fig. S2). The experimental criteria for good crystallinity of

445 the secondary product have been investigated through a separate experiment at elevated

446 temperature and time, which will be part of another paper.

447 Equant granular phases of non-phyllosilicate chemistry (Fig. 4E), in both experimental

448 setups, have low Mg and high Fe (Table 4). Such features are observed at the advanced stage

449 of reaction progress after the expanse of Mg from the solution. Crovisier et al. (1992)

450 performed thermodynamics calculations for basalt alteration in a closed system. They showed

451 that the advanced state of smectite formation ($[SiO_2/MgO]_{glass}$ / $[SiO2/MgO]_{secondary\ product}$ = 1)

452 is coupled with Ca-Al phases.

453 **4.3 Chemical affinity and kinetics evolution with coupled dissolution-precipitation**

454 **reaction**

455 Numerous studies have been performed to propose appropriate models of minerals and

456 glass dissolution (Daux et al., 1997; Techner et al., 1998; Techer et al., 2001; Hermanska et al.,

457 2023). An accurate model to describe kinetics of dissolution requires intrinsic thermodynamic

458 properties of mineral/rock, which depends on composition and internal structure, making any

459 model challenging to fit for glass dissolution study as degree of polymerisation (internal

460 structure) is specific to each glass. Although Hermanska et al. (2023) proposed a kinetic model

461 for dissolution rate estimation of basalt glass in open systems, which are from equilibrium, a

462 closed system still requires deeper insights. As closed system evolves, the cations released from

463 dissolution reach equilibrium and start fractionating into solid, resulting in a quasi-steady state

464 for certain cations. Alekseyev et al. (1997); Zhu et al. (2009) and Zhu et al. (2010) explained

465 the change in the dissolution rate (r-ΔG_r relationship) of feldspar in closed system by coupled

466 dissolution and precipitation. A dissolution reaction starts as far from equilibrium system and

467 may reach to equilibrium. According to the transition state theory, as dissolution reaction

468 progresses towards equilibrium, the rate decreases (r), and ΔG_r approaches zero. However, this

469 theoretical trend has not been experimentally observed by Techer et al. (2001) for basalt glass

470 dissolution in a closed system. We measured ΔG_r for each reaction step and correlated it with

471 the dissolution rate.

472   The reaction of basalt dissolution in alkaline conditions can be written as:

473 $(Si_1Al_{0.29}Ti_{0.04}Fe_{0.17}Mg_{0.22}Ca_{0.24}Na_{0.09}K_{0.01}O_{3.24}) + 2.12H_2O + 1.12H^+ + 0.28e^- =$

474 $H_4SiO_4^o + 0.29Al\,(OH)_4^- + 0.09Na^+ + 0.24Ca^{+2} + 0.01K^+ + 0.17Fe^{+3} + 0.04Ti\,(OH)_5^-$ (9)

475   The ion activity at each sampling step was calculated using PHREEQC. The ΔG_r of each

476 reaction step has been calculated following Techer et al. (2001) (see Appendix A supplementary

477 material, Section S3, Chemical Affinity Calculation, Table S2- S8). The dissolution rate and

478 ΔG_r relation is similar (Fig. 8) to Techer et al. (2001) observation.

479   The speciation and solubility modelling for each reaction step (Fig. 7) shows that brucite

480 remains in equilibrium from the beginning of the reaction. Based on the elemental evolution

481 study in the current experiment (Fig. 3), brucite can be considered a solid that precipitates from

482 the beginning and remains saturated or incorporated for a more extended reaction period. We

483 modified the total reaction affinity calculation by keeping the brucite, basalt, and reacting

484 solution in equilibrium (see Appendix A supplementary material, Section S3, Chemical Affinity

485 Calculation). The ΔG_r at the advanced stage of reaction reaches a value of -37.4 kcal/mole (36–

486 56 µm) and -34.8 kcal/mol (<36 µm). The ΔG_r for brucite precipitation is 33.8 kcal/mole, and

487 the total Gibbs free energy of the system (total reaction affinity) reaches 0.8–3 kcal/mol. This

488 suggests that incorporating thermodynamical parameters for precipitating phases explains the

489   earlier shift of chemical affinity curve with rate, in accordance with TST. Hence, fit refinement

490   can be done by incorporating the thermodynamic parameters of amorphous phases (Fig. 8).

491   The complete reaction, which can explain the basalt and water interaction energetics and

492   kinetics according to TST in a closed system can be expressed as a coupled dissolution and

493   dissolution reaction:

494    $(Si_1Al_{0.29}Ti_{0.04}Fe_{0.17}Mg_{0.22}Ca_{0.24}Na_{0.09}K_{0.01}O_{3.24}) + 2.12H_2O + 1.12H^+ + 0.28e^- =$

495    $H_4SiO_4^o + 0.29Al\,(OH)_4^- + 0.09Na^+ + 0.24Ca^{+2} + 0.01K^+ + 0.17Fe^{+3}$

496    $+ 0.04Ti\,(OH)_5^- + brucite$ (10)

497   **4.4 Comparison between open and closed system kinetics and limitations of extrapolation**

498   Numerous studies have investigated the kinetics of open systems, which are far from

499   equilibrium. Daux et al. (1997) showed that open systems reach equilibrium with decrease in

500   the flow rate, subsequently dissolution rate also decliness. A closed system can numerically be

501   extrapolated as an open system with an infinitesimally slow flow rate. The kinetics of closed

502   systems are orders of slower than open systems, which are far from equilibrium. Near

503   equilibrium, coupled dissolution and precipitation is responsible for slow kinetics, which also

504   explains the large difference in field and laboratory rates of dissolution (Zhu et al., 2004, 2009,

505   2010). Zhu et al. (2010) attempted to extrapolate a closed system (Ganor et al., 2007) to an

506   open system through reactive transport modelling in 1D, assuming single clay precipitation

507   along with primary mineral dissolution and reported time and space variability of saturation

508   index (SI) of phases with constant dissolution and precipitation rate. The current study

509   experimentally shows the possibility of multiple phases precipitation from single primary rock

510   dissolution. The precipitation of multiple amorphous precursors and chemical evolution with

511   increasing extent of dissolution poses substantial limitations for establishing r- ΔG_r

512   relationship.

4.5 Geochemical implications

Basalt dissolution kinetics measured in laboratory experiments under open-system conditions have shown a few orders of faster rates for natural conditions, where the rate is measured using palagonite thickness (Gislason and Arnorsson, 1993; Gislason and Eugster, 1987b; Techer et al., 2001). This discrepancy in rate has been explained by long-time interaction in natural conditions (Parruzot et al., 2015). However, the current study adds another possibility of basalt dissolution in a closed system within the natural terrain, as the rate lowers by two orders within 24 days. This study holds importance given many recent studies highlighting enhanced rock weathering of basalt as a potential strategy for CDR (Beearling et al., 2020, 2024; Goll et al., 2021; Viene et al.,2022).

4.5.1 Impact of poor drainage on CDR potential by ERW of basalt

Basalt dissolution rate in open systems with flow-rate high enough to maintain system far from equilibrium at steady state, remains higher. In contrast, the dissolution rate attains lower values with a decreasing flow rate. A closed system experiences an evolution in dissolution rates starting at a higher rate when the system approaches equilibrium or quasi-steady state, due to coupled dissolution and precipitation, the kinetics of dissolution lowers by two orders in 24 days. The total cations released by basalt glass dissolution increase at the same rate as glass dissolution until equilibrium is achieved and cations start fractionating in the precipitating phases. Any estimation based on total released cations due to basalt glass dissolution may give erroneous results if the equilibrium condition has not been investigated and precipitation-related correction is not incorporated. Large-scale estimation of CDR potential by ERW needs incorporation of factors that can affect amount of bivalent cations released by weathering. Beerling et al. (2024) estimated the CDR potential through field-based experiments, where total cation lost from basalt was considered available for bicarbonate formation. Although Beerling and others' calculation method accounts the effect of closed

538   system kinetics evolution, as mass loss has been calculated from parent material, the

539   fractionation of bivalent cation has not been considered. The current study shows within 20

540   hrs, magnesium starts fractionating in the secondary product, and after 54 hrs, calcium starts

541   fractionating from the solution. We have calculated the projected amount of bivalent cations at

542   each step of reaction if basalt dissolution is considered with evolving kinetics according to

543   closed system, ignoring precipitation. We compared it with measured values of bivalent cations

544   (see Appendix A. supplementary material Section S6), which accounts both kinetics evolution

545   as well as precipitation. The total amount of bivalent cations, after 400 hrs, remains 10 times

546   lower than calculations-based estimation (see Fig. 9). Although this study signifies the

547   importance of closed system-based calculations, it still cannot be strictly applied to any

548   cropland, without soil textural information. The natural weathering regimes vary between an

549   ideal closed system, poor drainage (full water storage) and an ideal open system, good drainage

550   (full discharge). Hence, a realistic calculation of CDR potential by ERW of basalt glass in any

551   cropland requires information about drainage system, which implies water residence time.

552   **4.5.2 Other implications of basalt glass alteration study in closed system**

553   The current study provides crucial laboratory evidence to the theoretical model proposed

554   by Crovisier et al. (1992) for basalt alteration in a closed system in volcanic terrains like

555   Iceland. Although the reaction advance did not reach the extent of zeolite formation, the

556   mineralisation sequence supports the continuously evolving nature of 2:1 clay chemistry. This

557   observation could explain the heterogeneity in the clay chemistry in soils having multiple dry

558   and wet cycles in poor drainage, as the reaction will be reset to a new extent due to dilution

559   each time. In volcanic terrains, a significant proportion of precipitation remains trapped as it

560   percolates into fissures and joints or is confined to volcanic craters, calderas, and local

561   depressions, resulting in lakes. Results of this study explain the nucleation pathways of neo-

562   formation of clay in active volcanic fields where the basalt surface remains heated enough so

563 that water does not evaporate, but interacts with basalt in the joints and fissures, paving the

564 paths of secondary mineralisation, e.g. bole beds formed in Deccan provinces (Sriwastava et

565 al., 2023). The experimental condition also helps understand the mineralisation pathways in

566 alkaline lakes, which are reported as sites for prebiotic life (Toner and Catling, 2019, 2020).

567 The information on element sequestration in secondary mineral nucleation over time greatly

568 impacts the biogeochemistry of alkaline lake environment, especially microbialites formation,

569 during the geochemical evolution of early earth. This study also holds importance for

570 understanding the origin of clay rich beds in the volcanic terrains of Mars due to alteration of

571 basaltic fragments (Treiman et al., 2015; Thorpe et al., 2022).

572

573 **5. Conclusions**

574 This study investigated basalt and water interaction at high time resolution (hour scale)

575 under poor drainage conditions; our results show that nucleation of secondary products starts

576 within 20 hours of the onset of the reaction, thus paving the way for the initial surface

577 nucleation. Brucite nucleation at an early stage indicates a strong control on the chemistry of

578 honeycomb-shaped smectites that precipitated later. At geological time scale, such observation

579 highlights the crucial importance of closed system (shorter duration) studies demonstrating the

580 first step towards alteration reaction before the system continues as closed, open or mixed later.

581 The cations released as a result of basalt glass dissolution may or may not be available for

582 further utilisation in bicarbonate formation due to interruption by precipitation, affecting the

583 potential of CDR by basalt dissolution in natural weathering regime. The major findings of this

584 study are summarised as follows:

585 1) Within 20 hours, brucite-like structures are the first secondary product that reaches

586 precipitation during basalt glass alteration in a closed system, followed by 2:1 clay structure

587 precursor, grown epitaxially over the sheet-like structure of brucite. This implies that the time

required in a closed system to affect the pathway of any alteration reaction is very small at a geological time scale, suggesting the important role of a closed system at each site for alteration studies.

2) The initial dissolution rate in a closed system drops by 100 times in 24 days.

3) The total amount of measured bivalent cations, after 400 hrs of basalt glass dissolution in a closed system, remains 10 times lower than estimated values without considering precipitation, suggesting an overestimation of CRD potential by ERW of basalt.

Appendix A. Supplementary materials Saturation index calculated for each reaction step, XRD of secondary product, IR spectra of secondary product has been provided as Table S1, Fig. S1 and Fig. S2. Chemical affinity calculation of closed system has been shown afterwards which has been done in four steps. The calculation is shown in tables from Tables S2 -S8. Table S9-10 shows a calculation of Li incorporation in Mg-clay and its effect on concentration in the reacting solution. pH measured during reaction has been plotted against time and graph is shown as Gig. S3. Further formulas has been shown which are used to calculate CDR potential if precipitation is ignored.

613

Data Availability:

Data are available through Mendeley Data at: https://doi.org/10.17632/vz78n3wwfb.1

616

References

Aagaard, P., & Helgeson, H. C. (1982). Thermodynamic and kinetic constraints on reaction rates among minerals and aqueous solutions; I, Theoretical considerations. *American journal of Science, 282*(3), 237-285.

Advocat, T., Chouchan, J. L., Crovisier, J. L., Guy, C., Daux, V., Jegou, C., ... & Vernaz, E. (1997). Borosilicate nuclear waste glass alteration kinetics: chemical inhibition and affinity control. *MRS Online Proceedings Library (OPL)*, 506, 63.

Alekseyev, V. A., Medvedeva, L. S., Prisyagina, N. I., Meshalkin, S. S., & Balabin, A. I. (1997). Change in the dissolution rates of alkali feldspars as a result of secondary mineral precipitation and approach to equilibrium. *Geochimica et Cosmochimica Acta, 61*(6), 1125-1142.

Angeli, F., Gaillard, M., Jollivet, P., & Charpentier, T. (2006). Influence of glass composition and alteration solution on leached silicate glass structure: a solid-state NMR investigation. *Geochimica et Cosmochimica Acta, 70*(10), 2577-2590.

Banfield, J. F., Jones, B. F., & Veblen, D. R. (1991). An AEM-TEM study of weathering and diagenesis, Abert Lake, Oregon: II. Diagenetic modification of the sedimentary assemblage. *Geochimica et Cosmochimica Acta, 55*(10), 2795-2810.

Bas, M. L., Maitre, R. L., Streckeisen, A., Zanettin, B., & IUGS Subcommission on the Systematics of Igneous Rocks. (1986). A chemical classification of volcanic rocks based on the total alkali-silica diagram. *Journal of petrology, 27*(3), 745-750.

Beerling, D. J., Kantzas, E. P., Lomas, M. R., Wade, P., Eufrasio, R. M., Renforth, P., ... & Banwart, S. A. (2020). Potential for large-scale CO2 removal via enhanced rock weathering with croplands. *Nature*, 583(7815), 242-248.

645

646 Beerling, D. J., Epihov, D. Z., Kantola, I. B., Masters, M. D., Reershemius, T., Planavsky, N.
647   J., ... & Banwart, S. A. (2024). Enhanced weathering in the US Corn Belt delivers
648   carbon removal with agronomic benefits. *Proceedings of the National Academy of*
649   *Sciences*, *121*(9), e2319436121.

650

651 Berger, G., Claparols, C., Guy, C., & Daux, V. (1994). Dissolution rate of a basalt glass in
652   silica-rich solutions: implications for long-term alteration. *Geochimica et*
653   *Cosmochimica Acta, 58*(22), *4875-4886*.

654

655 Berger, G., Schott, J., & Guy, C. (1988). Behaviour of Li, Rb and Cs during basalt glass and
656   olivine dissolution and chlorite, smectite and zeolite precipitation from seawater:
657   experimental investigations and modelisation between 50 and 300° C. *Chemical*
658   *Geology, 71*(4), 297-312.

659

660 Berger, G., Schott, J., & Loubet, M. (1987). Fundamental processes controlling the first stage
661   of alteration of a basalt glass by seawater: an experimental study between 200 and 320°
662   C. *Earth and Planetary Science Letters, 84*(4), 431-445.

663

664 Berner, R. A. (1978). Rate control of mineral dissolution under earth surface
665   conditions. *American Journal of Science, 278*(9), 1235-1252.

666

667 Bettison-Varga, L., & Mackinnon, I. D. (1997). The role of randomly mixed-layered
668   chlorite/smectite in the transformation of smectite to chlorite. *Clays and Clay*
669   *Minerals, 45*, 506-516.

670

671 Bouakkaz, R., Abdelouas, A., El Mendili, Y., Grambow, B., & Gin, S. (2016). SON68 glass
672   alteration under Si-rich solutions at low temperature (35–90° C): kinetics, secondary
673   phases and isotopic exchange studies. *Rsc Advances, 6*(76), 72616-72633.

674

675 Bourcier, W. L., Ebert, W. L., & Feng, X. (1992). Modelling surface area to volume effects on
676   borosilicate glass dissolution. *MRS Online Proceedings Library (OPL), 294*, 577.

677

Brown, K. (2011, May). Thermodynamics and kinetics of silica scaling. In *International Workshop on Mineral Scaling* (p. 8). Manila, Philippines.

Chakoumakos, B. C., Loong, C. K., & Schultz, A. J. (1997). Low-temperature structure and dynamics of brucite. *The Journal of Physical Chemistry B*, *101*(46), 9458-9462.

Christidis, G. E. (2006). Genesis and compositional heterogeneity of smectites. Part III: Alteration of basic pyroclastic rocks—A case study from the Troodos Ophiolite Complex, Cyprus. *American Mineralogist, 91*(4), 685-701.

Crovisier, J. L., Honnorez, J., & Eberhart, J. P. (1987). Dissolution of basaltic glass in seawater: Mechanism and rate. *Geochimica et Cosmochimica Acta*, *51*(11), 2977-2990.

Crovisier, J. L., Advocat, T., Petit, J. C., & Fritz, B. (1988a). Alteration of basaltic glass in Iceland as a natural analogue for nuclear waste glasses: geochemical modelling with DISSOL. *MRS Online Proceedings Library (OPL)*, *127*, 57.

Crovisier, J. L., Atassi, H., Daux, V., Honnorez, J., Petit, J. C., & Eberhart, J. P. (1988b). A new insight into the nature of the leached layers formed on basaltic glasses in relation to the choice of constraints for long term modelling. *MRS Online Proceedings Library (OPL)*, *127*, 41.

Crovisier, J. L., & Daux, V. (1990). Populations of clays formed by alteration of subglacial hyaloclastites from Iceland. *Chemical Geology, 84*(1-4), 261-263.

Crovisier, J. L., Advocat, T., & Dussossoy, J. L. (2003). Nature and role of natural alteration gels formed on the surface of ancient volcanic glasses (Natural analogs of waste containment glasses). *Journal of Nuclear Materials, 321*(1), 91-109.

Crovisier, J. L., Honnorez, J., Fritz, B., & Petit, J. C. (1992). Dissolution of subglacial volcanic glasses from Iceland: laboratory study and modelling. *Applied Geochemistry, 7*, 55-81.

709

710 Cuadros, J., Afsin, B., Jadubansa, P., Ardakani, M., Ascaso, C., & Wierzchos, J. (2013).
711   Microbial and inorganic control on the composition of clay from volcanic glass
712   alteration experiments. *American Mineralogist*, *98*(2-3), 319-334.

713

714 Curti, E., Crovisier, J. L., Morvan, G., & Karpoff, A. M. (2006). Long-term corrosion of two
715   nuclear waste reference glasses (MW and SON68): A kinetic and mineral alteration
716   study. *Applied Geochemistry, 21*(7), 1152-1168.

717

718 Daux, V., Crovisier, J. L., Hemond, C., & Petit, J. C. (1994). Geochemical evolution of basaltic
719   rocks subjected to weathering: fate of the major elements, rare earth elements, and
720   thorium. *Geochimica et Cosmochimica Acta, 58*(22), *4941-4954*.

721

722 Daux, V., Guy, C., Advocat, T., Crovisier, J. L., & Stille, P. (1997). Kinetic aspects of basaltic
723   glass dissolution at 90° C: role of aqueous silicon and aluminium. *Chemical*
724   *Geology, 142*(1-2), 109-126.

725

726 De La Fuente, S., Cuadros, J., Fiore, S., & Linares, J. (2000). Electron microscopy study of
727   volcanic tuff alteration to illite-smectite under hydrothermal conditions. *Clays and Clay*
728   *Minerals, 48*(3), 339-350.

729

730 Decarreau, A., Vigier, N., Pálková, H., Petit, S., Vieillard, P., & Fontaine, C. (2012).
731   Partitioning of lithium between smectite and solution: An experimental
732   approach. *Geochimica et Cosmochimica Acta*, *85*, 314-325.

733

734 Declercq, J., Diedrich, T., Perrot, M., Gislason, S. R., & Oelkers, E. H. (2013). Experimental
735   determination of rhyolitic glass dissolution rates at 40–200° C and 2< pH<
736   10.1. *Geochimica et Cosmochimica Acta*, *100*, 251-263.

737

738 Dehouck, E., McLennan, S. M., Meslin, P. Y., & Cousin, A. (2014). Constraints on abundance,
739   composition, and nature of X-ray amorphous components of soils and rocks at Gale
740   crater, Mars. *Journal of Geophysical Research: Planets, 119*(12), 2640-2657.

741

742 Dessert, C., Dupré, B., François, L. M., Schott, J., Gaillardet, J., Chakrapani, G., & Bajpai, S.
743   (2001). Erosion of Deccan Traps determined by river geochemistry: impact on the
744   global climate and the $^{87}Sr/^{86}Sr$ ratio of seawater. *Earth and Planetary Science*
745   *Letters, 188*(3-4), 459-474.

746 Dessert, C., Dupré, B., Gaillardet, J., François, L. M., & Allègre, C. J. (2003). Basalt
747   weathering laws and the impact of basalt weathering on the global carbon cycle.
748   *Chemical Geology, 202*(3-4), 257-273.

750 Eggleton, R. A., Foudoulis, C., & Varkevisser, D. (1987). Weathering of basalt: changes in rock
751   chemistry and mineralogy. *Clays and Clay Minerals, 35*, 161-169.

753 Fang, Q., Lu, A., Hong, H., Kuzyakov, Y., Algeo, T. J., Zhao, L., ... & Chorover, J. (2023).
754   Mineral weathering is linked to microbial priming in the critical zone. *Nature*
755   *Communications, 14*(1), 345.

757 Fiore, S., Huertas, F. J., Huertas, F., & Linares, J. (2001). Smectite formation in rhyolitic
758   obsidian as inferred by microscopic (SEM-TEM-AEM) investigation. *Clay*
759   *Minerals*, *36*(4), 489-500.

761 Fox, L. E. (1988). The solubility of colloidal ferric hydroxide and its relevance to iron
762   concentrations in river water. *Geochimica et Cosmochimica Acta, 52*(3), 771-777.

764 Frings, P. J., & Buss, H. L. (2019). The central role of weathering in the geosciences. *Elements:*
765   *An International Magazine of Mineralogy, Geochemistry, and Petrology*, *15*(4), 229-
766   234.

768 Ghiara, M. R., Franco, E., Petti, C., Stanzione, D., & Valentino, G. M. (1993). Hydrothermal
769   interaction between basaltic glass, deionized water and seawater. *Chemical*
770   *Geology*, *104*(1-4), 125-138.

772 Gin, S., Ryan, J. V., Schreiber, D. K., Neeway, J., & Cabié, M. (2013). Contribution of atom-
773   probe tomography to a better understanding of glass alteration mechanisms:
774   Application to a nuclear glass specimen altered 25 years in a granitic
775   environment. *Chemical Geology, 349*, 99-109.

776

Gislason, S. R., & Arnórsson, S. (1993). Dissolution of primary basaltic minerals in natural waters: saturation state and kinetics. *Chemical Geology*, *105*(1-3), 117-135.

Gislason, S. R., & Eugster, H. P. (1987a). Meteoric water-basalt interactions. I: A laboratory study. *Geochimica et Cosmochimica Acta*, *51*(10), 2827-2840.

Gislason, S. R., & Eugster, H. P. (1987b). Meteoric water-basalt interactions. II: A field study in NE Iceland. *Geochimica et Cosmochimica Acta, 51*(10), *2841-2855*.

Gislason, S. R., & Oelkers, E. H. (2003). Mechanism, rates, and consequences of basaltic glass dissolution: II. An experimental study of the dissolution rates of basaltic glass as a function of pH and temperature. *Geochimica et Cosmochimica Acta*, *67*(20), 3817-3832.

Goll, D. S., Ciais, P., Amann, T., Buermann, W., Chang, J., Eker, S., ... & Vicca, S. (2021). Potential CO2 removal from enhanced weathering by ecosystem responses to powdered rock. *Nature Geoscience*, *14*(8), 545-549.

Grambow, B., Jercinovic, M. J., Ewing, R. C., & Byers, C. D. (1985). Weathered basalt glass: a natural analogue for the effects of reaction progress on nuclear waste glass alteration. *MRS Online Proceedings Library (OPL), 50*, 263.

Guy, C., & Schott, J. (1989). Multisite surface reaction versus transport control during the hydrolysis of a complex oxide. *Chemical Geology, 78*(3-4), 181-204.

Heřmanská, M., Voigt, M. J., Marieni, C., Declercq, J., & Oelkers, E. H. (2023). A comprehensive and consistent mineral dissolution rate database: part II: secondary silicate minerals. *Chemical Geology, 636*, 121632.

Keller, W. D., Reynolds, R. C., & Inoue, A. (1986). Morphology of clay minerals in the smectite-to-illite conversion series by scanning electron microscopy. *Clays and Clay Minerals, 34*, 187-197.

810 Kump, L. R., Brantley, S. L., & Arthur, M. A. (2000). Chemical weathering, atmospheric CO_2,
811   and climate. *Annual Review of Earth and Planetary Sciences, 28*(1), 611-667.

812

813 Lasaga, A. C., Soler, J. M., Ganor, J., Burch, T. E., & Nagy, K. L. (1994). Chemical weathering
814   rate laws and global geochemical cycles. *Geochimica et Cosmochimica Acta, 58*(10),
815   *2361-2386*.

816

817 Leturcq, G., Berger, G., Advocat, T., & Vernaz, E. (1999). Initial and long-term dissolution
818   rates of aluminosilicate glasses enriched with Ti, Zr and Nd. *Chemical Geology, 160*(1-
819   2), 39-62.

820

821 Loock, S., van Wyk de Vries, B., & Hénot, J. M. (2010). Clinker formation in basaltic and
822   trachybasaltic lava flows. *Bulletin of volcanology, 72*, 859-870.

823

824 Meng, J., Liu, X., Li, B., Zhang, J., Hu, D., Chen, J., & Shi, W. (2018). Conversion reactions
825   from dioctahedral smectite to trioctahedral chlorite and their structural
826   simulations. *Applied Clay Science, 158*, 252-263.

827

828 Meunier, A., Petit, S., Cockell, C. S., El Albani, A., & Beaufort, D. (2010). The Fe-rich clay
829   microsystems in basalt-komatiite lavas: importance of Fe-smectites for pre-biotic
830   molecule catalysis during the Hadean eon. *Origins of Life and Evolution of*
831   *Biospheres*, *40*(3), 253-272.

832

833 Murphy, W. M., Oelkers, E. H., & Lichtner, P. C. (1989). Surface reaction versus diffusion
834   control of mineral dissolution and growth rates in geochemical processes. *Chemical*
835   *Geology, 78*(3-4), 357-380.

836

837 Nagy, K. L., & Lasaga, A. C. (1992). Dissolution and precipitation kinetics of gibbsite at 80°
838   C and pH 3: The dependence on solution saturation state. *Geochimica et Cosmochimica*
839   *Acta, 56*(8), *3093-3111*.

840

841 Nagy, K. L., Blum, A. E., & Lasaga, A. C. (1991). Dissolution and precipitation kinetics of
842   kaolinite at 80° C and pH 3; the dependence on solution saturation state. *American*
843   *Journal of Science, 291*(7), 649-686.

844

845 Neeway, J. J., Kerisit, S. N., Liu, J., Zhang, J., Zhu, Z., Riley, B. J., & Ryan, J. V. (2016). Ion-
846   exchange interdiffusion model with potential application to long-term nuclear waste
847   glass performance. *The Journal of Physical Chemistry C, 120*(17), 9374-9384.

848

849 Nesbitt, H. W., & Wilson, R. E. (1992). Recent chemical weathering of basalts. American
850   *Journal of science, 292*(10), 740-777.

851

852 Oelkers, E. H., & Gislason, S. R. (2001). The mechanism, rates and consequences of basaltic
853   glass dissolution: I. An experimental study of the dissolution rates of basaltic glass as a
854   function of aqueous Al, Si and oxalic acid concentration at 25° C and pH= 3 and
855   11. *Geochimica et cosmochimica acta, 65*(21), 3671-3681.

856

857 Parkhurst, D. L., & Appelo, C. A. J. (1999). User's guide to PHREEQC (Version 2): A computer
858   program for speciation, batch-reaction, one-dimensional transport, and inverse
859   geochemical calculations. *Water-resources investigations report, 99*(4259), 312.

860

861 Parruzot, B., Jollivet, P., Rébiscoul, D., & Gin, S. (2015). Long-term alteration of basaltic glass:
862   Mechanisms and rates. *Geochimica et Cosmochimica Acta, 154*, 28-48.

863

864 Paul, A. (1977). Chemical durability of glasses; a thermodynamic approach. *Journal of*
865   *materials science, 12*, 2246-2268.

866

867 Rinder, T., & von Hagke, C. (2021). The influence of particle size on the potential of enhanced
868   basalt weathering for carbon dioxide removal-Insights from a regional
869   assessment. *Journal of Cleaner Production, 315*, 128178.

870

871 Rowe, M. C., & Brewer, B. J. (2018). AMORPH: A statistical program for characterizing
872   amorphous materials by X-ray diffraction. *Computers & geosciences, 120*, 21-31.

873

874 Schuiling, R. D., & Krijgsman, P. (2006). Enhanced weathering: an effective and cheap tool to
875   sequester CO_2. *Climatic Change, 74*(1), 349-354.

876

877 Shannon, R. D. (1976). Revised effective ionic radii and systematic studies of interatomic distances in halides and chalcogenides. *Acta crystallographica section A: crystal physics, diffraction, theoretical and general crystallography*, *32*(5), 751-767.

881 Spanos, N., & Koutsoukos, P. G. (1998). Kinetics of precipitation of calcium carbonate in alkaline pH at constant supersaturation. Spontaneous and seeded growth. *The Journal of Physical Chemistry B*, *102*(34), 6679-6684.

885 Sriwastava, P., Singh, V. V., Mathew, G., Kogure, T., & Myneni, S. (2023). Origin of clays in the interbasaltic red boles of Deccan Volcanics: Pedogenesis versus palagonitization. *Applied Clay Science, 246*, 107183.

889 Stefánsson, A., & Gíslason, S. R. (2001). Chemical weathering of basalts, Southwest Iceland: effect of rock crystallinity and secondary minerals on chemical fluxes to the ocean. *American Journal of Science, 301*(6), 513-556.

893 Strefler, J., Amann, T., Bauer, N., Kriegler, E., & Hartmann, J. (2018). Potential and costs of carbon dioxide removal by enhanced weathering of rocks. *Environmental Research Letters*, *13*(3), 034010.

897 Taylor, L. L., Driscoll, C. T., Groffman, P. M., Rau, G. H., Blum, J. D., & Beerling, D. J. (2020). Increased carbon capture by a silicate-treated forested watershed affected by acid deposition. *Biogeosciences Discussions*, *2020*, 1-29.

901 Techer, I., Advocat, T., Lancelot, J., & Liotard, J. M. (2001). Dissolution kinetics of basaltic glasses: control by solution chemistry and protective effect of the alteration film. *Chemical Geology, 176*(1-4), 235-263.

905 Techner, I., Advocat, T., Vernaz, E., Lancelot, J. R., & Liotard, J. M. (1998). Dissolution rate equations for basaltic glasses. Comparison with experimental data. *Mineral Mag A*, *62*, 1498-1499.

Thorpe, M.T., Bristow, T.F., Rampe, E.B., Tosca, N.J., Grotzinger, J.P., Bennett, K.A., Achilles, C.N., Blake, D.F., Chipera S.J., Downs, G., Downs, R.T., Morrison, S.M., Tu, V., Castle, N., Craig, P., Marais, D.J.D., Hazen, R.M., Ming, D.W., Morris, R.V., Treiman, A.H., Vaniman, D.T., Yen, A.S., Vasavada, A.R., Dehouck, E., Bridges, J.C., Berger, J., McAdam, A., Peretyazhko, T., Siebach, K.L., Bryk, A.B., Fox, V.K., & Fedo, C.M. (2022) Mars Science Laboratory CheMin data from the Glen Torridon region and the significance of lake-groundwater interactions in interpreting mineralogy and sedimentary history. *Journal of Geophysical research: Planets, 127*(11), e2021JE007099

Toner, J. D., & Catling, D. C. (2019). Alkaline lake settings for concentrated prebiotic cyanide and the origin of life. *Geochimica et Cosmochimica Acta, 260,* 124-132.

Toner, J. D., & Catling, D. C. (2020). A carbonate-rich lake solution to the phosphate problem of the origin of life. *Proceedings of the National Academy of Sciences, 117*(2), 883-888.

Treiman, A.H., Bish, D.L., Vaniman, D.T., Chipera, S.J., Blake, D.F., Ming, D.W., Morris, R.V., Bristow, T.F., Morrison, S.M., Baker, M.B., Rampe, E.B., Downs, R.T., Filiberto, J., Glazner, A.F., Gellert, R., Thompson, L.M., Schmidt, M.E., Deit, L.L., Weins, R.C., McAdam, A.C., Achilles, C.N., Edgett, K.S., Farmer, J.D., Fendrich, K.V., Grotzinger, J.P., Gupta, S., Morookian, J.M., Newcomb, M.E., Rice, M.S., Spray, J.G., Stolper, E.M., Sumner, D.Y., Vaavada, A.R., & Yen, A.S. (2016). Mineralogy, provenance, and diagenesis of a potassic basaltic sandstone on Mars: ChemMin X-rat diffraction of the Windjana sample (Kimberley area, Gale Crater). *Journal of geophysics Research: Planets, 121*(1), 75-106

Tsipursky, S. I., & Drits, V. A. (1984). The distribution of octahedral cations in the 2: 1 layers of dioctahedral smectites studied by oblique-texture electron diffraction. *Clay minerals*, *19*(2), 177-193.

Velde, B. B., & Meunier, A. (2008). The origin of clay minerals in soils and weathered rocks. *Springer Science & Business Media*.

Vernaz, E., Gin, S., Jégou, C., & Ribet, I. (2001). Present understanding of R7T7 glass alteration kinetics and their impact on long-term behavior modeling. *Journal of Nuclear Materials, 298*(1-2), 27-36.

943

944   Vienne, A., Poblador, S., Portillo-Estrada, M., Hartmann, J., Ijiehon, S., Wade, P., & Vicca, S.

945   (2022). Enhanced weathering using basalt rock powder: carbon sequestration, co-

946   benefits and risks in a mesocosm study with Solanum tuberosum. *Frontiers in*

947   *Climate, 4*, 869456.

948

949   Wojdyr, M. (2010). Fityk: a general-purpose peak fitting program. *Journal of applied*

950   *crystallography, 43*(5), 1126-1128.

951

952   Wolff-Boenisch, D., Gislason, S. R., Oelkers, E. H., & Putnis, C. V. (2004). The dissolution

953   rates of natural glasses as a function of their composition at pH 4 and 10.6, and

954   temperatures from 25 to 74 C. *Geochimica et Cosmochimica Acta, 68*(23), 4843-4858.

955   Zhu, C., Blum, A. E., & Veblen, D. R. (2004). Feldspar dissolution rates and clay precipitation

956   in the Navajo aquifer at Black Mesa, Arizona, USA. *Water-rock interaction, 11*, 895-

957   899.

958   Zhu, C., & Lu, P. (2009). Alkali feldspar dissolution and secondary mineral precipitation in

959   batch systems: 3. Saturation states of product minerals and reaction paths. *Geochimica*

960   *et Cosmochimica Acta, 73*(11), 3171-3200.

961

962   Zhu, C., Lu, P., Zheng, Z., & Ganor, J. (2010). Coupled alkali feldspar dissolution and

963   secondary mineral precipitation in batch systems: 4. Numerical modeling of kinetic

964   reaction paths. *Geochimica et Cosmochimica Acta, 74*(14), 3963-3983.

965

966 **List of Figures**

56 μm experiment. Circular and diamond shapes indicate the spots for analytical measurement in <36 μm and 36-56 μm experiments, respectively. Plain circles and diamonds indicate the features with phyllosilicate equivalent chemistry. Circles and diamonds with vertical bars indicate features with non-phyllosilicate chemical signatures. (A) Honeycomb morphology of secondary product grown as coating of basalt glass surface (B) Aggregate of ellipsoid and equant granular phases. (C) Honeycomb morphology of secondary product. (D) Equant aggregate and equant granular-shaped secondary product.

Fig-5 Evolution of elemental ratios with time, showing congruency and incongruency stages during dissolution. (A) Variation of Al, Mg, and Ca ratio with respect to Si during the entire extent of reaction. Circular dots indicate elemental ratio in fluid, and lines indicate ratio in basalt rock. The colours of the symbols are specific to the elements. (B) Li and Si ratio evolution with time. The blue dot indicates the ratio in reacting solution, while the orange dot indicates the constant value in basalt glass.

Fig-6 Normalised mass loss plot to time. The blue diamond indicates the experiment with <36 μm fraction of basalt glass. The orange square indicates an experiment with a 36-56 μm fraction of basalt glass.

Fig-7 Saturation index versus time for reaction setup with grain size (36-56 μm). Solid lines show minerals that reach the oversaturation state during the reaction; the colours are specific to the mineral variety. Coloured bands in the background of the image mark the zone of oversaturation of the specific mineral mentioned within the coloured band.

Fig-8 Variation of total reaction affinity (ΔG_r) with dissolution rate (r) corresponding to each step of reaction. The dotted blue line indicates the expected theoretical trend between total reaction affinity and rate, according to transition state theory (TST). The orange diamond indicates an experiment with a 36-56 μm fraction of glass, and the blue circle indicates an experiment with <36 μm glass. The greenish band showed the experimental data when reaction affinity was calculated according to the consideration in Techer et al. (2001), which results in a shift in ΔG_r in the negative direction. The yellow band shows the experimental points data when total reaction affinity was calculated considering brucite in equilibrium with the reacting solution and basalt.

Fig-9 Amount of bivalent cations (Ca+Mg) in fluid interacting with basalt glass in a closed system. Measured values are sum of the concentrations of Ca and Mg at each reaction step. The calculated amount of bivalent cations results when secondary precipitation is not considered, and total cations released from basalt are estimated from a normalised mass loss rate. The calculated values automatically incorporate effect of precipitation on rates of dissolution in closed system.

List of tables

Table-1 : Experimental setup

Table-2 : Glass composition

Table-3 : Elemental Composition evolution in both experimental setups (<36 μm and 36-56 μm)

Table-4 : Chemical composition of secondary products formed in both sets of experiments.

1   **Experimental pathways of clay formation and kinetics of basalt alteration**

2   **in poor drainage systems: Implications for weathering**

3   **Piyush Sriwastava[1,2], Vijay Kumar Saini[1,3], George Mathew[1]*, Anil D. Shukla[4]**

4   [1]Department of Earth Sciences, Indian Institute of Technology Bombay, Mumbai,
5   Maharashtra 400076, India
6   [2]Museum of Natural History, University of Oxford, Parks Road, Oxford, OX1 3PW, UK
7   [3]Helmholtz-Zentrum Dresden-Rossendorf e. V.- Institute of Resource Ecology, Bautzner Landstraße 400, 01328
8   Dresden, Germany
9   [4]Physical Research Laboratory, Ahmedabad, Gujarat 380059, India

10

11   **Abstract**

12   Basalt being the most dominant rock on the earth's crust, contributes significantly to the global

13   elemental cycle through~~by its~~ weathering. In recent years, the potential of basalt weathering

14   has been continuously scrutinized as a carbon di-oxide removal (CDR) strategy. An accurate

15   estimation of such ~~large~~ large-scale processes requires a deeper insight ~~of~~into the mechanism

16   controlling the basalt glass dissolution under field conditions. This contribution assesses the

17   chemical evolution of fluid interacting with basalt glass in poorly drained regimes. Experiments

18   showed a drop in kinetics of alteration ($r_0 = 1.7 \times 10^{-9}$ mol.m^{-2}. s^{-1}) by two orders of magnitude

19   in 24 days and emphasiz~~s~~es the onset of secondary mineral formation within 20 hr of the start

20   of dissolution~~a reaction~~. At first, Mg starts fractionating from the solution due to brucite

21   oversaturation and reaches undersaturation after 60th hour due to onset of other Mg-bearing

22   minerals. From the 54th hour, montmorillonite remains oversaturated until Mg is

23   ~~complet~~entirely consumed by precipitation~~exhausts from the system~~ at the 164th hour. SEM-

24   EDS investigation shows the presence of two major morphologies of secondary products: (a)

25   honeycomb shape (smectite), with high Mg (>3 wt%) and octahedral composition similar

26   [(Si/Al+Fe+Mg) and Al/Si] to smectite, (b) aggregate of ellipsoid and/or equant granular

27   phases. Compositionally, elliptical and granular aggregates show affinity towards low Mg and

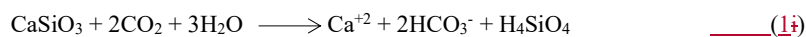28   high Fe variety of smectite amorphous precursor. The absence of pure brucite grains indicates

29   epitaxial growth of Mg-rich, honeycomb-shaped phyllosilicate precursor on the brucite

30   template due to well-reported structural similarity between the brucite layer and 2:1

31   phyllosilicate octahedral sheet. Elliptical and equant-shaped grains with or without

32   compositional similarity with smectite phases have high Fe and low Mg, indicating their

33   formation under a low Mg concentration stage in solution. Precipitation of the secondary

34   phases at various stages of reaction progress affects the total reaction affinity in a closed

35   system. Coupled dissolution and precipitation at the fluid-rock interface isare responsible for

36   lowering the kinetics of dissolution reactions in a closed system, previously explaining the slow

37   kinetics of natural weathering regimes. The damped kinetics of dissolution and cations

38   fractionation in secondary products within a few hours of onset of dissolution reaction can

39   result in an over–estimation (ten times) of CDR potential estimation by enhanced rock

40   weathering (ERW) if calculations does not involves the nature of closed system evolution

41   during basalt glass alteration.

42

45
46   *Corresponding Author: gmathew@iitb.ac.in

1. Introduction:

Silicate weathering, viz., disintegration and decomposition of rock, drives the element cycle on earth surface (Frings and Buss, 2019). Ions released during chemical weathering have two crucial fates: (1) carried away by river from catchment or (2) captured in neoformed secondary minerals, e.g., clays, carbonates or metal (oxy)hydroxide (Velde and Meunier, 2008), that are vital for organisms nutrient turnover (Fang et al., 2023). Rivers in basaltic terrain have shown the highest cationic flux due to highly reactive constituents in basalt such as amorphous interstitial glass, pyroxene and olivine (Eggleton et al., 1987; Nesbitt and Wilson, 1992; Hermanska et al., 2023) resulting $30 – 35\%$ of global CO_2 fixation in the form of bicarbonates of cations, that later lead to carbonate precipitation (Dessert et al., 2003). The dominant pathway of carbon dioxide removal (CDR) by weathering of basalt can be expressed by chemical reaction:

$$CaSiO_3 + 2CO_2 + 3H_2O \longrightarrow Ca^{+2} + 2HCO_3^- + H_4SiO_4 \qquad (1)$$

Basalt weathering has not only significant control over the long-term CO_2 content in atmosphere but also on global cycle of elements and chemistry of earth's critical zone (Kump et al., 2000; Dessert et al., 2001; Stefansson and Gislason, 2001). The rate of CO_2 fixation can be increased by enhanced kinetics of basalt dissolution (Schuiling and Krijgsman, 2006), which is achieved by addition of finely crushed basalt (Goll et al., 2021; Rinder and Hagke, 2021; Vienne et al., 2022). Beerling et al. (2020), Strefeler et al. (2018) and Taylor et al. (2016) have demonstrated that enhanced weathering of basaltic rock can be adopted as potential CO_2 removal strategies as it can capture 10.5 ± 3.8 t CO_2 ha^{-1} (Beerling et al., 2024) if applied in croplands which also enhances the food security and crop productivity. According to reaction (1), the large-scale estimation of CDR potential will directly depend on bivalent cations supply rate and residence time, which depends on the kinetics of basalt dissolution and proximity of the system to equilibrium or precipitation conditions, respectively. Most of the large-large-scale

72 calculations are based on basalt dissolution models under open systems, which are far from

73 equilibrium~~, while~~. ~~N~~natural weathering in near~~—~~surface environments~~regimes~~ ~~are~~is

74 dominated by poor drainage systems, where fluid ~~does not liberate fluid-rock interface quickly~~

75 ~~and~~leads to coupled dissolution and precipitation at the fluid-rock interface.

76 ~~——~~Numerous studies have been done to understand initial basalt dissolution

77 kinetics over a wide range of temperatures and pH in an open system (e.g. Gislason and Eugster,

78 1987a; Guy and Schott, 1989; Crovisier et al., 1988a, 1988b, 1990, 1992, 2003; Daux et al.,

79 1994, 1997). Oelker and Gislason (2001)~~;~~ and Heřmanská et al. (2023) have proposed an

80 empirical formula to calculate the steady state rate (r) of basalt glass dissolution in an open

81 system, far from the equilibrium. However, ~~While~~basalt dissolution in a closed system

82 ~~i~~remains ~~s~~less probed. Daux et al. (1997) ~~-~~studied basalt dissolution kinetics evolution using

83 multiple open systems with high flow rates resulting far from equilibrium systems and low

84 flow rates resulting near equilibrium systems analogous to closed systems. Following transition

85 state theory, the steady-state rate of each reaction setup strongly correlated with reactions Gibbs

86 free energy (ΔG_r). ~~For the first time,~~Techer et al. (2001)~~ for the first time,~~ investigated the

87 general dissolution model~~,~~ based on TST~~,~~ to explain the basalt dissolution kinetics in a closed

88 system approaching equilibrium. However, the relationship between kinetic evolution ~~with~~and

89 total chemical affinity remains unexplained. Although closed systems kinetics evolution ~~have~~

90 has been understood for mi~~i~~nerals like alkali feldspar with coupled dissolution-precipitation

91 during alteration reaction in a closed system (Alekseyev et al., 1997; Zhu and Lu, 2009; Zhu

92 et al., 2010), ~~but~~such an approach requires a mechanistic understanding for basaltic glass.

93 According to current understanding, basalt interaction with water starts with H_2O~~water~~

94 diffusion and hydration of a silicate network followed by a metal proton exchange reaction,

95 resulting in a hydrated glass layer (Bourcier et al., 1992; Angeli et al., 2006). Initially, the

96 diffusion rate is higher than the hydrolysis rate; eventually, with increasing thickness of the

Formatted: Subscript

97 hydrated glass layer, diffusion rates slow down to the hydrolysis rate, and the dissolution

98 reaction becomes congruent (Gislason and Eugster, 1987; Crovisier., 1992). Hydrolysis at

99 higher temperatures occurs partially, resulting in a porous surface layer facilitating diffusion

100 (Berger et al., 1987, 1988, 1994), while hydrolysis is total at low temperatures. Neeway et al.

101 (2016) have proposed an alkali interdiffusion model based on Fick's law for quantitatively

102 constraining the diffusion parameters. Bouakkaz et al. (2016) studied glass (SON68)

103 dissolution in an open system (flow-through reactor) using ^{29}Si doped fluid and showed that

104 ~~glass dissolution is governed by both diffusion and surface alteration reaction~~both diffusion

105 and surface alteration reactions govern glass dissolution. Bouakkaz and others~~They also~~

106 reported that the hydrated glass layer is Mg-poor. Secondary products are Mg-rich silicates,

107 indicating a unique role of Mg during glass alteration reaction, as envisaged in the present

108 work. Since basalt dissolution kinetics is controlled by surface reactions (Berner, 1978; Murphy

109 et al., 1989), many researchers have attempted to establish a general relation between reaction

110 rates and chemical affinity under Transition State Theory (TST), considering the desorption of

111 different surface complexes as a rate-defining step. Grambow (1985) considered desorption of

112 purely siliceous surface complex as a rate-defining step and proposed first-order rate law,

113 which is a function of proton activity in solution [H$^+$] and activity of orthosilicic acid [H$_4$SiO$_4$].

114 Berger et al. (1994) considered =SiOH as a precursor species, and the basalt dissolution rate

115 was a function of 0.33 power of Q/K, where Q is precursor species activity, and K is amorphous

116 silica hydrolysis reaction's solubility constant. The power value (0.33) in this rate calculation

117 equation depends on the silica retention amount in the alteration gel, which varies with

118 temperature. Daux et al. (1997) studied the dissolution kinetics of basalt at 90°C and considered

119 hydrolysis of a hydrated glass layer with composition Si, Al, Fe and H$_2$O as a determining step.

120 Although numerous attempts have been made to unveil the mechanism of basalt dissolution

121 and establish kinetics relations in an open system, the fate of ions released in a closed system

122 needs investigation from the perspective of kinetics evolution, the effect of equilibrium on

123 kinetics and pathways of secondary mineral formation.

124   Hence, the current study has investigated the pathways of basalt glass alteration in

125 alkaline conditions under a closed system as water bodies in basaltic terrain become alkaline

126 (Gislason et al., 1996; Reimers et al., 1996; Dessert et al., 2001; Pokrovsky et al., 2005). We

127 have used basalt glass rather than a crystalline rock ~~due to two specifie~~for two reasons: (1) each

128 crystallised basalt contains variable amounts of ~~amount of~~ interstitial glass a~~long with~~nd

129 crystalline components. The dissolution rate of glass being faster than crystalline controls the

130 pathways of precipitation reaction, (2) to bridge the knowledge gap of glass dissolution

131 mechanism and kinetics, which is crucial for reaction path modelling of normal basalt in which

132 the crystalline components, e.g., pyroxene and plagioclase have been well understood.

133   In the present contribution~~study~~, we have evaluated the following two problems

134 associated with basalt glass alteration in closed-system that hold importance from the

135 perspective of a new strategy of CDR using ERW of basalt glass: 1) Evolution of alteration

136 kinetics, ΔG_r and pathways of secondary mineral formation in a closed alkaline system and 2)

137 The disparity between dissolution rate estimation and total reaction affinity in a closed system

138 following TST, explained by coupled dissolution and precipitation reactions. We have also

139 estimated the impact of poor drainage conditions on CDR potential.

140

141 **2.   Material and Methods:**

142 **2.1.   Sample preparation**

143   The basalt glass used in this study is a natural glass collected from Hawaii Island. It was

144 ground using agate mortar to increase the reactive surface area. The ground sample was sieved

145 to obtain 36–56 µm and less than 36 µm size fraction. The 36 –56 µm fraction was cleaned

146 with ultrasonic bath to remove the ultra-fine particles. First, cleaning was done for 10 minutes

Formatted: Font: 12 pt
Formatted: Font: 12 pt

147 in deionised water, followed by acetone. Five to six cleaning cycles with water and acetone

148 were sufficient to remove all fine particles from 36–56 μm fraction. Subsequently, the sample

149 was dried overnight at 60°C.

150 **2.2 Experiment Setup**

151 The experiment was performed in a custom-made setup (Fig.1). A closed four-necked

152 round bottom flask was equipped with a temperature sensor probe connected to the solution

153 and a PID controller. The flask was kept on a heating mantle, having a rounded opening with

154 woven fabric in the surroundings, to heat homogeneously. The heater system and PID controller

155 were synced to maintain the system's temperature within the ±1°C range. A mechanical stirrer

156 was employed in the reaction setup to keep the reacting grains of basalt glass in suspension

157 throughout the reaction. There was a retractable outlet system and a PTFE syringe of 5 ml

158 connected with a flexible teflon pipe. 1.25 ml of the solution was piped out at regular intervals.

159 Each sample was filtered using a 0.2 μm cellulose filter before analysis. After each sampling

160 step, outlet systems were cleaned and dried to avoid contamination from the previous sample.

161 The reaction was kept at 90°C with a 1:500 rock-water ratio (0.6 g rock in 300 ml solution).

162 Graham condenser was attached to flask with a sealed top to condense vapour and avoid ~~an~~

163 ~~increase of~~increased pressure in the reaction chamber. The pH of the reacting solution was

164 measured at regular intervals by inserting a pH-measuring electrode connected to a digital

165 meter. pH measurement was calibrated for 90°C. The starting fluid was slightly alkaline, with

166 a pH of 8.3. Reacting alkaline fluid was prepared using NaOH (Merck) in milli-Q water.

167 **2.3 Analytical Methods**

168 The surface area of the grains was measured using Brunauer-Emmett-Teller Method

169 (BET). The crystalline and amorphous nature of basalt glass and the secondary clay products

170 was evaluated with ~~amorphousity of basalt glass and mineralogy of secondary product was~~

171 ~~studied using~~ X-ray diffraction (XRD). The crystal chemistry of raw glass and the secondary

172 product was studied using Fourier transform infrared (FTIR) spectroscopy. Textural,

173 morphological and analytical study of sub-micron-sized secondary product was performed

174 under scanning electron microscopy (SEM) with energy dispersive X-ray spectroscopy (EDS).

175 The chemical composition of fluid and basalt glass was determined using ~~Inductively~~inductive

176 coupled plasma atomic emission spectroscopy (ICP-AES) and mass spectroscopy (MS).

177 The specific surface area of the samples was measured on Quantachrome Nova 2000e at

178 the University of Vienna, Austria, using the six-point Brunauer-Emmett-Teller (BET) method.

179 The sample with grain size 36–56µm has a surface area of 4.51 ± 0.01 $m^2 g^{-1}$, while sample with

180 grain size <36 µm has a surface area of 6.38 ± 0.33 $m^2.g^{-1}$. The X-ray diffraction (XRD) analysis

181 was performed at the Department of Earth Sciences, Indian Institute of Technology (IIT)

182 Bombay, with Empyrean Panalytical XRD. X-ray was generated with a Cu target. The X-ray

183 spectra were collected with 0.01° step increment and a count time of 58.395 s per step using

184 Cu Kα radiation transmitted through 0.04 rad soller slit opening and 1.52 mm anti-scatter slit.

185 The diffracted beam was detected using a PIXcel^{3D} detector.

186 The Fourier transform infrared (FTIR) measurements were performed on Thermo Nicolet

187 6700 and Bruker Vertex 80 FTIR systems at the Department of Earth Sciences and

188 Sophisticated Analytical Instrument Facility (SAIF), IIT Bombay. Sample powder was mixed

189 with KBr (2 mg of sample and 200 mg of KBr), and a pressed disc was prepared. Spectra were

190 collected in the range of 400–4000 cm^{-1} with a resolution of 2 cm^{-1}. The decomposition of OH-

191 stretching bands into component peaks was done using fityk 1.3.1 software (Wojdyr, 2010). It

192 uses the Levenberg-Marquardt method for curve fitting. Curve fitting parameters were

193 accepted based on a weighted sum of squared residuals (WSSR) parameters and agreement

194 between calculated and experimental profiles.

195 The ~~The reacting solution~~solution's ~~'s~~ Na, K, Ca, Mg, Al, and Si concentrations ~~in the~~

196 ~~solution~~ were measured using Spectro Arcos Inductively coupled plasma atomic emission

197 spectroscopy (ICP-AES) at SAIF, IIT Bombay. The instrument was calibrated for 0.1 ppm to

198 100 ppm using a multielement standard prepared by serial dilution. The precision and accuracy

199 of the analysis were better than 5%, and the blanks were negligible. Accuracy and precision

200 were continuously monitored using standard as unknown. The detection limit of the instrument

201 was 0.01 ppm. Lithium concentration in the basalt glass and reacting fluid was measured using

202 ThermoIcap quadrupole Inductively coupled plasma mass spectroscopy (ICP-MS) at the

203 Department of Earth Sciences, IIT Bombay. BHVO-2 (Hawaiian basalt), RGM-2 (Rhyolite

204 from Glass Mountain), STM-2 (Syenite), SBC-1 (Brush Creek shale), and SCO-2 (Cody shale)

205 rock standards were used for calibration and accuracy during the Li concentration measurement

206 of basalt glass. Rock standards and basalt glass were digested using microwave acid digestion

207 technique. Reacting fluid chemical analysis was calibrated using multielement standards of

208 different concentrations, prepared by serial dilution. Precision and accuracy in both analyses

209 were below 5%.

210   Imaging of submicron to sub-nano meter sized secondary product of basalt glass

211 alteration reaction was done at Physical Research Laboratory (PRL) India, using a scanning

212 electron microscope (SEM) (model JEOL IT300). Insitu compositional measurement was done

213 under an energy dispersive spectrometer (EDS) attached to SEM. An ion sputtering coater was

214 used to create a conductive carbon layer before imaging to avoid charging in SEM. In situ

215 chemistry of basalt glass grains was measured at the Department of Earth Sciences, IIT

216 Bombay (India), using a Cameca SX-50 electron microprobe analyser (EPMA) with five

217 wavelength dispersive spectrometers. Glass grains were mounted in epoxy stubs and finely

218 polished. Carbon coating was done before analysis under EPMA to avoid charging. Analysis

219 was done using a pointed probe (diameter 2 μm) at an acceleration voltage of 15 kV and a fixed

220 probe current of 20 nA.

221 **2.4 Geochemical Modelling:**

222   PHREEQC computer program (C++ language) was used to perform aqueous

223   geochemical calculations at low temperatures (Parkhurst and Appelo 1999). Speciation and

224   solubility geochemical modelling was done for each reaction step (sample) to calculate product

225   minerals' saturation indices (SI). The molar concentration of elements in each sampled

226   solution, fluid temperature, pH, and volume were used as input parameters to calculate the

227   activity of chemical species. The Graham condenser attached to the chamber maintained

228   pressure at 1 atm in the reaction chamber. Hence, the modelling parameter for pressure was set

229   by default as 1 atm. The simulated pH was also compared with the experimentally measured

230   pH (see Table S4 and Table S5). The activity of chemical species was used to calculate the

231   Gibbs free energy of each reaction step (ΔG_r). The Carbfix and MINTEQ databases wasere

232   used in the modelling.

233   **2.5 Dissolution rate determination:**

234   The kinetics of dissolution is a measure of rate of mass dissociation from reactant.

235   Element concentration continuously increases during dissolution in a closed system, while an

236   open system results in a mechanical steady state of elements defined by flow rate. The amount

237   of element released in the solution at any stage of the reaction can measure the dissolved mass

238   of basalt glass if the element does not fractionate in any secondary product. Many researchers

239   have considered Li as a tracer element for dissolution studies (Vernaz et al., 2001; Techer et al.,

240   2001; Curti et al., 2006; Gin et al., 2013; Parruzot et al., 2015). Li concentration and changed

241   solution volume were used after fluid removal in the previous sampling step to calculate the

242   mass loss of basalt during dissolution. Normalised mass loss (NML) measures mass loss per

243   unit surface area of reacting basalt. It can be calculated using the following equation:

244

245        $$\text{Normalised Mass Loss (NML)} = ({}^{n}C_{Li} \times {}^{n}V) / (R_{Li} \times S) \qquad (2\text{1})$$

246    ${}^{n}C_{Li}$ = concentration of Li in fluid at n^{th} hour

247 ^nV = volume of fluid at n^{th} hour

248 R_{Li} = concentration of Li in rock

249 S = total surface area (m^2g^{-1})

250 The alteration rate of basalt glass for each sampling step can be measured using the difference

251 between normalised mass loss in two consecutive steps and the time gap between them. The

252 formula to measure alteration rate in "mole m^{-2} s^{-1}" can be written as follows:

253

254 Alteration rate $r_{[i+(i+1)]/2}$ = [$(NML)^{i+1}$ – $(NML)^i$] / [$(t^{i+1} - t^i)$ × (molecular mass) .....(3~~2~~)

255

256 **2.6 Gibbs free energy calculation:**

257 In recent years, mineral dissolution kinetics has been investigated using transition state

258 theory. Nagy et al. (1991), Nagy and Lasaga (1992), Lasaga et al. (1994) proposed a model to

259 study kinetics by incorporating "reaction affinity" term in ΔG_r measurement ($A = -\Delta G_r$):

260
$$r = k^+ \left(\prod_J a_J^{m_J} f(\Delta G_r) \right) \tag{4}$$

261 r is the mineral dissolution rate, k+ is the rate constant, $\prod_J a_J^{m_J}$ shows the activity product of

262 species in the solution, $f(\Delta G_r)$ is the Gibbs free energy function, which can be expressed as

263 follows (Aagaard and Helgeson, 1982; Nagy et al., 1991; Lasaga et al., 1994):

264
$$f(\Delta G_r) = 1- \exp(n\ \Delta G_r/RT) \tag{5}$$

265 For the current experimental setup, we measured Gibbs free energy of each incremental

266 reaction with dissolution of basalt glass using the following equation:-

267
$$Q/K_e = \exp(\Delta G_r/RT) \tag{6~~3~~}$$

268 Q is the ion activity product, K_e is the solubility product, R is the ideal gas constant, T is the

269 temperature, and ΔG_r is the reaction Gibbs free energy. The final rate equation used was:

$$R = k^+(1 - Q/K_e) \tag{7}$$

Following Paul (1977), basalt glass solubility product (K_e) was calculated by considering glass

a mixture of oxide. x_i (molar fraction) and K_i (solubility products) of each oxide are known.

Hence, the solubility of glass has been calculated using ideal solid solution relation (Bourcier

et al., 1992; Advocat et al., 1997; Leturcq et al., 1999):

$$\log K_e = \sum_i x^i \log K^i + \sum_i x^i \log x^i \tag{84}$$

3. Results:

3.1 Basalt Glass Characterisation

The Hawaiian basalt glass powder X-ray diffraction (XRD) pattern has no discernible

peaks, indicating the absence of crystalline phases. XRD spectra showed a broad low-intensity

hump in the range of 25–30° 2θ (Fig. 2A), characteristic of amorphous material (Dehouck et

al., 2014; Rowe and Brewer, 2018;). The specific surface area (SSA) of basalt glass, in size

range <36 µm, is 6.38 ± 0.33 m^2/g; comparatively, 36-56 µm size fraction has a lower, $4.51 \pm$

0.01 m^2/g, specific surface area (measured using the BET method) (Table1). SEM images of

basalt grains show several characteristic morphological features of amorphous glass, e.g.,

conchoidal fractures, blocky irregular surfaces, etc. (Loocks et al., 2010). Under an electron

microscope, glass grains appear micro-pores or pits-free. BSE images (Fig. 2C) of glass

fragments under EPMA show homogeneous grey shades across all grains, suggesting a lack of

compositional heterogeneity within and between the grains. The bulk chemistry of basaltic

glass measured with ICP-AES shows that almost all element's concentration lies within the 1σ

range of 25 grains chemistry measured under EPMA (Table 2). This confirms the

compositional homogeneity of basaltic glass fragments and discards the possibility of site-

specific variation in the glass dissolution reaction due to chemical heterogeneity of the reacting

substrate within a system. The total alkali in glass ($K_2O + Na_2O = 2.87$ wt%) is less than 5

294   wt%, and SiO$_2$ (52.50 wt%) lies between 45 and 54 wt%, which is in the range of basalt as per

295   the TAS diagram of rock classification (Bas et al., 1986). FeO (t), MgO, Al$_2$O$_3$, TiO$_2$, and CaO

296   also lies in the range of basalt. Li concentration in the basalt glass is 5.27 ppm (Table 2).

297   **3.2 Evolution of pH and elements in fluid**

298   The experiment started with slightly alkaline fluid (pH=8.7) under a closed system.

299   Unlike previous studies in open systems (far from equilibrium), closed systems show a

300   dynamic evolution in the fluid composition (Crovisier, 1987, 1988a, 1988b; Daux, 1997;

301   Techer et al., 2001; Oelker and Gislason, 2001; Gislason and Oelker, 2003; Wolff-Boenisch,

302   2004; Declercq et al., 2013). The pH increases rapidly and reaches a plateau at 9.35-9.40 within

303   48 hours of the reaction. After 284 hours, pH drops to an initial value of ~8.5 and remains

304   almost constant from 300 hours onwards (Table 3). Lithium (Li) concentration in the basalt

305   glass is in trace amount (~5 ppm). As Li is highly mobile, it liberates from reacting solid quickly

306   and does not fractionate to any secondary phase. The concentration of Li in both dissolution

307   experiments shows an overall trend of increase with time (Table 3), reaching a value of 4 ppb

308   in 548 hours.

309   The Fe concentration was below the detection limit of analysis. This experimental setup

310   has oxidation conditions similar to recent earth's surface. Under oxidising conditions, iron

311   attains a ferric state (Fe^{+3}) and goes into solid phases, e.g., iron (oxy) hydroxide, resulting in

312   very low Fe^{+3} (aq) (Fox, 1988). Other than Fe, all major cations present in basalt (Na, K, Ca,

313   Si, Mg and Al) have been measured in reacting fluid to monitor the dissolution reaction and

314   subsequent fluid evolution in both experiments. Na, K increases rapidly compared to Ca, Mg,

315   Al and Si in the first few hours under both experimental setups (Fig. 3). Except for Mg, other

316   cations (Na, K, Ca, Al and Si) reach their local maximum concentration after 54 hours, followed

317   by a sudden decrease within 6 hours (Fig. 3). After 60 hours, cations (Na, K, Ca, Al and Si)

318   concentration in solution continuously increases with different trends. The elemental

concentration evolution of Mg behaves differently. Mg reaches a plateau value of ~1.70 ppm at 20 hours and remains almost the same till 54 hours. This is followed by a continuous drop in concentration, which is contemporary to other cations' concentration drop stage until Mg concentration exceeds the detection limit. The time of Mg disappearance from the solution differs in both experiments, 164 hours in <36 μm and 236 hours in 36–56 μm. Cations show a change in the concentration increment behaviour from the Mg loss point in the solution. This concentration evolution pattern is similar in both experimental conditions.

3.3 Secondary products

Pre-experimental characterisation of glass surfaces has been performed in detail. Submicron features have been investigated under an analytical electron microscope (SEM-EDS). SEM imaging of basalt glass surface in both experiments shows secondary products in the form of coating. The morphologies of secondary products can be categorised into two major types: a) honeycomb-like structure grown on the glass surface (Fig. 4 A, C) and b) equant and/or ellipsoid grains accumulated on the surface (Fig. 4 B, D). In both experiment setups, these features are present with varying chemical compositions and assemblages, encompassing the signature of reaction progress associated with their formation (Table 4).

In the experiment with <36 μm glass fraction, a secondary product having honeycomb morphology is a dominant phase with a size of up to a few microns (Fig. 4 A). In Fig. 4A, the sporadic presence of small particles with honeycomb structures attached to the large grain surface indicates a smaller fraction of the original basalt glass. Chemically, both features have similar compositions and are slightly modified to the initial basalt glass (Table 4). Cation ratios, Si/(Al+Mg+Fe) and Al/Si, based on 11 oxygen, lie between 1-2 and 0-0.4, respectively, depicting a close chemical affinity towards nontronite or saponite type of 2:1 phyllosilicate (Fig. 4 E) (Cuadros et al., 2013). Other secondary products in this experiment setup are aggregates of phases with ellipsoidal morphology and equant granular morphology (Fig. 4B).

344 Chemically, ellipsoid phases have Si/(Al+Mg+Fe) between 1-2 and Al/Si > 0.4, which can be

345 compositionally categorised as montmorillonite (2:1 phyllosilicate) (Fig. 4E). Ellipsoid phases

346 are Mg depleted and K enriched compared to honeycomb morphology (Table-4). Equant

347 granular phases, co-existing with ellipsoidal morphotypes (Fig. 4B), are smaller in size (<0.5

348 microns) with relatively lower Fe, Mg and Ti with increased anions (oxygen) wt%, suggesting

349 calcium-aluminium hydrous silicates (CAHS). The cation ratios, 2<Si/(Al+Mg+Fe)<1 and

350 Al/Si>1, fall out of the 2:1 phyllosilicate range (Fig. 4E).

351   In the experiment with 36-56 μm glass grains, secondary products having honeycomb

352 morphology are dominant phases grown as glass surface coating. Chemically, these phases are

353 Fe (>17 wt%), Mg (>3 wt%) and Ca (> 9wt%) enriched, with Si/Al+Mg+Fe (between 1-2) and

354 Al/Si (< 0.4) values showing close affinity to nontronite/saponite, 2:1 phyllosilicate (Fig. 4E).

355 Other secondary products are sub-nano-meter phases with equant growth. Based on their

356 morphology, they could be categorised into two major types: (1) Equant aggregate phase and

357 (2) Equant granular phase (Fig. 4D). Although equant aggregate phases show a compositional

358 similarity with nontronite and saponite (Fig. 4E) because Si/(Al+Mg+Fe) lies between 1-2 and

359 Al/Si <0.4, but Mg (<3 %) is lower than honeycomb-shaped phases (Table-4). Equant granular

360 phases are found at glass surfaces as isolated nano to micron-size mounds. They do not show

361 chemical affinity towards any 2:1 phyllosilicate, Si/(Al+Mg+Fe), and Al/Si lies out of the range

362 for phyllosilicate (Fig. 4E). High Fe (average 43 wt.%, n=5), Ti and low Mg, Si are distinct

363 compositional identities of equant granular phases.

364

365 **4. Discussion**

366 **4.1 Dissolution behaviour and kinetics**

367   Dissolution reaction under an open system attains a steady state far from equilibrium,

368 resulting in no precipitation. Hence, mobile cations, e.g. Na and K, were used as a proxy to

369 measure the extent of dissolution in open systems (Daux et al., 1997; Techer et al., 2001).

370 Closed systems reach equilibrium due to a continuous increase in the elemental concentration,

371 resulting in the precipitation of saturated phases and causing the fractionation of elements in

372 the solid against the release in the solution. After an extent of reaction progress, closed systems

373 experience a combination of dissolution and precipitation, ~~emphasizing application of~~requiring

374 a highly mobile element~~s~~ (Li) as a proxy to calculate the dissolution extent, behaviour and

375 kinetics. Although Li is highly mobile, it can substitute Mg in the octahedral clay sites due to

376 similarity in ionic radii (Shannon, 1976). Li fractionation in the current experimental condition,

377 calculated based on expression of partition coefficient ($\log D_{Li}$) proposed by Decarreau et al.

378 (2012), is within the error of Li concentration measurement for quadrupole (Q)-ICPMS (see

379 Table S9 and Table S10). Note that this calculation is based on expression proposed for

380 hectorite (Li-Mg clay). The current experimental product's Mg concentration (~4%) is lower,

381 leading to a lower partition coefficient.

382 The Li concentration measured at each step of dissolution reaction gives the extent to

383 which basalt glass was dissolved (using eqn 1). Both size fractions of basalt glass show a

384 similar trend of normalised mass loss variation during the entire extent of dissolution reaction

385 (Fig. 6). Smaller fraction (<36 μm) has higher values of normalised mass loss in comparison

386 to larger fractions (36–56 μm) at any extent of time (Fig. 6), due to larger surface area (Table-

387 1). Starting at 100 hours, normalised mass loss increases rapidly for both the fraction and slows

388 down afterwards. Mass loss evolution with time is exponential ($r^2 = 0.74$–0.77) (Fig. 6). Basalt

389 glass dissolution rate for a smaller fraction (<36 μm), calculated in the initial days of reaction,

390 is (r_0) 1.7×10^{-9} mole.m^{-2}.s^{-1}, which lowers by 100 times by the end of 24 days to (r) 5.7×10^{-11}

391 mole.m^{-2}.s^{-1}. The initial dissolution rate of a larger fraction is 2.5×10^{-9} mole.m^{-2}.s^{-1}and the final

392 rate (after 24 days) is 6.5×10^{-11} mole.m^{-2}.s^{-1}.

393   In both experimental setups, elemental evolution patterns with time are similar (Fig.

394   3). Elemental ratios (Li/Si, Al/Si, Mg/Si, Ca/Si) in reacting fluid show higher values in the

395   initial 20 hours (Fig. 5) for basalt glass, suggesting a preferential removal of modifier cations

396   in silicate structure due to proton-metal exchange reaction (Ghiara et al., 1993, Gin et al., 2013).

397   Such dissolution behaviour indicates an incongruent nature. The protonation of silicate

398   structure causes an increase in pH (Fig. S3). The ratio of Li/Si in fluid and basalt glass reaches

399   similar values after 20 hours (Fig. 5). It remains almost constant later, indicating the congruent

400   nature of the dissolution reaction afterwards, with minor fluctuations signifying the equilibrium

401   with saturated phases. Other cations (Al, Mg, Ca) ratio with Si in the fluid decreases below the

402   glass values (Fig. 5). It reaches a plateau, indicating preferential incorporation of these cations

403   in the precipitation of secondary phases.

404   **4.2 Secondary product formation mechanism: Implication towards phyllosilicate**

405   **nucleation**

406   Basalt glass dissolution reaction in a closed system has resulted in a continuously

407   evolving fluid chemistry (Fig. 3). Aqueous geochemical modelling of this dynamic system

408   shows the possible mineral phases undergoing supersaturation (see Table S1 for saturation

409   index) at each stage of reaction progress (Fig. 7). Despite the continuous dissolution of glass,

410   Mg concentration in the reacting solution reached a plateau within 20 hours, corresponding

411   with brucite [$Mg(OH)_2$] supersaturation (Fig. 7). Although brucite was an oversaturated phase

412   from the 4th hour onwards, according to thermodynamics, its precipitation started with a lag of

413   14 -16 hours due to nucleation delay associated with lower degree of supersaturation, called

414   induction period (Spanos and Koutsoukos, 1998; Brown, 2011). At 54th hour, a decrease of

415   elemental concentration, e.g. Al, Si, Ca along with Mg in the reacting solution signifies the

416   start of another solid phase, Ca-montmorillonite (smectite), indicating oversaturation (Fig. 7)

417   at this stage of the system. After 6 hours of brucite and smectite coprecipitation, Mg

418 concentration reaches below ~1 ppm, resulting in a brucite undersaturation state at 60th hour,

419 leaving smectite (Ca- montmorillonite) as the only saturated phase afterwards. The sudden

420 disappearance of montmorillonite (smectite) from an oversaturation state at the 160th hour

421 corresponds to Mg concentration below the detection limit (0.01 ppm). Record of element

422 concentration evolution and theoretical estimation of mineral supersaturation suggested two

423 ~~major~~significant stages of smectite precipitation in this system: (1) smectite (2:1 phyllosilicate)

424 coprecipitation with brucite and (2) only smectite precipitation.

425   SEM-EDS study of secondary products shows honeycomb-shaped features in both

426 experimental conditions with high Mg (>3 wt.%). Many researchers have reported the

427 honeycomb-shaped morphology as a characteristic feature of smectite (Keller et al., 1986;

428 Fiore et al., 2000; De La Fuente et al., 2000; Christidis, 2006). Compositionally, the honeycomb

429 structure is closely related to the nontronite and saponite smectite (Fig. 4E). Other secondary

430 products with smectite chemical affinity, e.g., the ellipsoidal and equant aggregate phases, have

431 low Mg and high Fe. None of the secondary phases observed has brucite chemistry (Fig. 4),

432 although fluid composition and thermodynamic modelling have shown a strong signature of

433 precipitation (Figs. 3,7). This suggests either the transformation/incorporation of brucite

434 structure into other stable phases or its dissolution, which should have shown an increased Mg

435 concentration. After the first appearance of brucite in the system, there was no signature of Mg

436 concentration increment, neglecting the dissolution hypothesis for the absence of brucite.

437 Several studies have shown that brucite-like structure is an intermediate stage of smectite

438 formation or transformation (Banfield et al., 1991; Bettison-Varga and Mackinnon, 1997;

439 Meunier et al., 2010; Meng et al., 2018) since brucite has structural similarity with octahedral

440 sheet of clay (Tsipursky and Drits, 1984; Chakoumakos et al., 1997). Hence, brucite constitutes

441 the perfect template for smectite epitaxial growth. Brucite oversaturation before

442 montmorillonite (smectite) saturation (Fig. 7) might facilitate high Mg smectite growth viz.

honeycomb shaped in both experimental conditions (Table-4). The smectite oversaturation without brucite (Fig. 7) might indicate the secondary product formation stage with low Mg, e.g. ellipsoid phase and equant aggregate (Fig. 4E). Powder x-ray diffractogram collected at the end of the experiment shows an absence of diffraction peaks (Fig. S1), suggesting secondary products as amorphous precursors for crystalline mineral varieties. The FTIR spectra of both the experimental products in the stretching region of OH vibration show metal-OH bonds overlayed by glass spectra (Fig. S2). The experimental criteria for good crystallinity of the secondary product have been investigated through a separate experiment at elevated temperature and time, which will be part of will be published as another separate paper.

Equant granular phases of non-phyllosilicate chemistry (Fig. 4E), in both experimental setups, have low Mg and high Fe (Table 4). Such features are observed at the advanced stage of reaction progress after the expanse of Mg from the solution. Crovisier et al. (1992) performed thermodynamics calculations for basalt alteration in a closed system. They showed that the advanced state of smectite formation ($[SiO_2/MgO]_{glass}$ / $[SiO2/MgO]_{secondary\ product}$ = 1) is coupled with Ca-Al phases.

4.3 Chemical affinity and kinetics evolution with coupled dissolution-precipitation reaction

Numerous studies have been performed to propose appropriate models of minerals and glass dissolution (Daux et al., 1997; Techner et al., 1998; Techer et al., 2001; Hermanska et al., 2023). An accurate model to describe kinetics of dissolution requires intrinsic thermodynamic properties of mineral/rock, which depends on composition and internal structure, making any model difficultchallenging to fit for glass dissolution study as degree of polymerisation (internal structure) is specific to each glass. Although, Hermanska et al. (2023) proposed a kinetic model for dissolution rate estimation of basalt glass in open systems, which are from equilibrium, a closed system still requires deeper insights. As a closed system evolves, the

468 cations released from dissolution reaches to equilibrium and starts fractionating in to solid,

469 resulting in a quasi- steady state for certain cations. Alekseyev et al. (1997); Zhu et al. (2009)

470 and Zhu et al. (2010) explained the change in the dissolution rate (r-ΔG_r relationship) of

471 feldspar in closed system by coupled dissolution and precipitation. A dissolution reaction starts

472 as far from equilibrium system and may reach to equilibrium. According to the transition state

473 theory, as dissolution reaction progresses towards equilibrium, the rate decreases (r), and an

474 increase in the reaction extent results in an increase in ΔG_r approaches to zero. and a decrease

475 in the dissolution rate (r)However, this theoretical trend has not been seen experimentally

476 observedvalid by Techer et al. (2001) for basalt glass dissolution in a closed system. We

477 measured ΔG_r for each reaction step and correlated it with the dissolution rate.

478   The reaction of basalt dissolution in alkaline conditions can be written as:

479 $(Si_1Al_{0.29}Ti_{0.04}Fe_{0.17}Mg_{0.22}Ca_{0.24}Na_{0.09}K_{0.01}O_{3.24}) + 2.12H_2O + 1.12H^+ + 0.28e^- =$

480     $H_4SiO_4^o + 0.29Al\ (OH)_4^- + 0.09Na^+ + 0.24Ca^{+2} + 0.01K^+ + 0.17Fe^{+3} + 0.04Ti\ (OH)_5^-$ (9ii)

481   The ion activity at each sampling step was calculated using PHREEQC. The ΔG_r of each

482 reaction step has been calculated following Techer et al. (2001) (see Appendix A supplementary

483 material, Section S3, Chemical Affinity Calculation, Table S2- S8). The dissolution rate and

484 ΔG_r relation is similar (Fig. 8) to Techer et al. (2001) observation.

485   The speciation and solubility modelling for each reaction step (Fig. 7) shows that brucite

486 remains in equilibrium from begithe beginning of the the reaction. Based on the elemental

487 evolution study in the current experiment (Fig. 3), brucite can be considered a solid that

488 precipitates from the beginning and remains saturated or incorporated for a more extended

489 reaction period. We modified the total reaction affinity calculation by keeping the brucite,

490 basalt, and reacting solution in equilibrium (see Appendix A supplementary material, Section

491 S3, Chemical Affinity Calculation). The ΔG_r at the advanced stage of reaction reaches a value

492 of -37.4 kcal/mole (36–56 μm) and -34.8 kcal/mol (<36 μm). The ΔG_r for brucite precipitation

493 is 33.8 kcal/mole, and the total Gibbs free energy of the system (total reaction affinity) reaches

494 0.8–3 kcal/mol. This suggests that incorporating thermodynamical parameters for precipitating

495 phases explains the earlier shift of chemical affinity curve with rate, in accordance with TST.

496 Hence, fit refinement can be done by incorporating the thermodynamic parameters of

497 amorphous phases (Fig. 8). The complete reaction, which can explain the basalt and water

498 interaction energetics and kinetics according to TST in a closed system can be expressed as a

499 coupled dissolution and dissolution reaction:
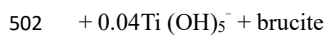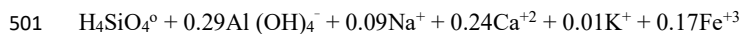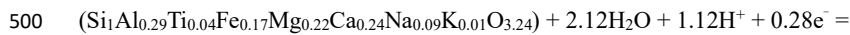
500 $(Si_1Al_{0.29}Ti_{0.04}Fe_{0.17}Mg_{0.22}Ca_{0.24}Na_{0.09}K_{0.01}O_{3.24}) + 2.12H_2O + 1.12H^+ + 0.28e^- =$

501 $H_4SiO_4^o + 0.29Al\,(OH)_4^- + 0.09Na^+ + 0.24Ca^{+2} + 0.01K^+ + 0.17Fe^{+3}$

502 $+ 0.04Ti\,(OH)_5^- + brucite$ ———

503 (10~~iii~~)

4.4 Comparison between open and closed system kinetics and limitations of extrapolation

505 Numerous studies have investigated the kinetics of open systems, which are far from

506 equilibrium. Daux et al. (1997) showed that ~~an~~ open system~~s~~ reach~~es near~~ equilibrium with

507 decrease in the flow rate, subsequently~~and~~ dissolution rate ~~also~~ also dec~~lines~~reases ~~with a~~

508 ~~decrease in the flow rate~~. A closed system can numerically be extrapolated as an open system

509 with an infinitesimally slow flow rate. The kinetics of closed systems are orders of slower than

510 open systems, which are far from equilibrium. Near equilibrium, coupled dissolution and

511 precipitation is responsible for slow kinetics ~~in a~~, which also explains the large difference in

512 field and laboratory rates of dissolution (Zhu et al., 2004, 2009, 2010). Zhu et al. (2010)

513 attempted to extrapolate a closed system (Ganor et al., 2007) to an open system through reactive

514 transport modelling in 1D, assuming single clay precipitation along with primary mineral

515 dissolution and reported time and space variability of saturation index (SI) of phases with

constant dissolution and precipitation rate. The current study experimentally shows the possibility of multiple ~~precipitation~~ phases precipitation from~~along with a~~ single primary rock dissolution. The precipitation of multiple amorphous precursors and chemical evolution with increasing extent of dissolution ~~reaction~~ poses substantial limitations for establishing r- ΔG_r relationship.

4.5 Geochemical implications

Basalt dissolution kinetics measured in laboratory experiments under open-system conditions have shown a few orders of faster rates for natural conditions, where the rate is measured using palagonite thickness (Gislason and Arnorsson, 1993; Gislason and Eugster, 1987b; Techer et al., 2001). This discrepancy in rate has been explained by long-time interaction in natural conditions (Parruzot et al., 2015). However, the current study adds another possibility of basalt dissolution in a closed system within the natural terrain, as the rate lowers by two orders within 24 days. This study holds importance ~~in the view of~~given many recent studies highlighting enhanced rock weathering of basalt as a potential strategy for CDR (Beearling et al., 2020, 2024; Goll et al., 2021; Viene et al.,2022).

4.5.1 Impact of poor drainage on CDR potential by ERW of basalt

Basalt dissolution rate in open systems with flow-rate high enough to maintain system far from equilibrium at steady state, remains higher ~~while~~. In contrast, the dissolution rate attains lower values with a decreasing flow rate. A closed system experiences an evolution in dissolution rates starting at a higher rate ~~and a~~ when ~~s~~the system approaches ~~to~~ equilibrium or quasi-steady state,~~-~~ ~~d~~Due to coupled dissolution and precipitation, the ~~the~~kinetics of dissolution lowers by two orders in 24 days ~~due to coupled dissolution and precipitation~~. The total cations released by basalt glass dissolution increase~~s~~ ~~with~~at the same rate as glass dissolution~~,~~ until equilibrium is achieved and cations start~~s~~ fractionating in the precipitating

phases. Any estimation based on total released cations ~~as a result of~~due to basalt glass dissolution may give erroneous result~~s~~ if the equilibrium condition ~~will~~has not been investigated and ~~precipitation~~ precipitation-related correction ~~will not be~~is not~~en~~ incorporated. ~~Large~~ Large-scale estimation of CDR potential by ERW needs incorporation of factors ~~which~~that can affect amount of bivalent cations released by weathering. Beerling et al. (2024) estimated the CDR potential through ~~field~~ field-based experiment~~s~~, where total cation lost from basalt was considered available for bicarbonate formation. Although Beerling and others' calculation ~~approach~~ method ~~takes care of~~accounts the effect of closed system kinetics evolution, ~~because~~ as mass loss has been calculated from parent material~~,~~, the~~and but~~ fractionation of bivalent cation has not been considered. ~~C~~The current study shows~~,~~ within 20 hrs~~,~~ magnesium starts fractionating in the secondary product, and after 54 hrs~~,~~ calcium starts fractionating from the solution. We have calculated the projected amount of bivalent cations at each step of reaction if basalt dissolution is considered with evolving kinetics according to closed system, ignoring precipitation. ~~but~~However, precipitation is ignored, and Ww~~e~~ compared it with measured values of bivalent cations (see Appendix A. supplementary material Section S6), which accounts both kinetics evolution as well as precipitation. The total amount of bivalent cations, after 400 hrs, remains 10 times lower than ~~calculations~~ calculations-based estimation (see Fig. 9). Although this study signifies the importance of closed ~~system~~ system-based calculations ~~but~~, it still ~~it~~ cannot be ~~exa~~strictly applied to any cropland, without soil textural information. The natural weathering regimes ~~varies~~ vary between an ideal closed system~~.~~ viz., poor drainage (~~full~~full ~~storage of water~~water storage) and an ideal open system, ~~viz.,~~ good drainage (full discharge). Hence, a realistic calculation of CDR potential by ERW of basalt glass in any cropland requires information about drainage system, which implies ~~to~~ water residence time.

———

4.5.2 Other implications of basalt glass alteration study in closed system

The current study provides crucial laboratory evidence to the theoretical model proposed by Crovisier et al. (1992) for basalt alteration in a closed system in volcanic terrains like Iceland. Although the reaction advance did not reach the extent of zeolite formation, the mineralisation sequence supports the continuously evolving nature of 2:1 clay chemistry. This observation could explain the heterogeneity in the clay chemistry in soils having multiple dry and wet cycles in poor drainage, as the reaction will be reset to a new extent due to dilution each time. In volcanic terrains, a significant proportion of precipitation remains trapped as it percolates into fissures and joints or is confined to volcanic craters, calderas, and local depressions, resulting in lakes. Results of this study explain the nucleation pathways of neo-formation of clay in active volcanic fields where the basalt surface remains heated enough so that water does not evaporate, but interacts with basalt in the joints and fissures, paving the paths of secondary mineralisation, e.g. bole beds formed in Deccan provinces (Sriwastava et al., 2023). The experimental condition also helps understand the mineralisation pathways in alkaline lakes, which are reported as sites for prebiotic life (Toner and Catling, 2019, 2020). The information on element sequestration in secondary mineral nucleation over time greatly impacts the biogeochemistry of alkaline lake environment, especially microbialites formation, during the geochemical evolution of early earth. This study also holds importance for understanding the origin of clay rich beds in the volcanic terrains of Mars, due to alteration of basaltic fragments (Treiman et al., 2015; Thorpe et al., 2022).

5. Conclusions

This study investigated basalt and water interaction at high time resolution (hour scale) under poor drainage conditions; our results show that nucleation of secondary products starts within 20 hours of the onset of the reaction, thus paving the way for the initial surface

nucleation. Brucite nucleation at an early stage indicates a strong control on the chemistry of honeycomb-shaped smectites that precipitated later. At geological time scale, such observation highlights the crucial importance of closed system (shorter duration) studies demonstrating the first step towards alteration reaction before the system continues as closed, open or mixed later. The cations released as a result of basalt glass dissolution may or may not be available for further utilisation in bicarbonate formation due to interruption by precipitation, affecting the potential of CDR by basalt dissolution in natural weathering regime. The major findings of this study are summarised as follows:

1) Within 20 hours, brucite-like structures are the first secondary product that reaches precipitation during basalt glass alteration in a closed system, followed by 2:1 clay structure precursor, grown epitaxially over the sheet-like structure of brucite. This implies that the time required in a closed system to affect the pathway of any alteration reaction is very small at a geological time scale, suggesting the important role of a closed system at each site for alteration studies.

2) The initial ~~rate of dissolution~~dissolution rate in a closed system drops by 100 times in 24 days.

3) The total amount of measured bivalent cations, after 400 hrs of basalt glass dissolution in a closed system, remains 10 times lower than estimated values without considering precipitation, suggesting an overestimation of CRD potential by ERW of basalt.

Appendix A. Supplementary materials Saturation index calculated for each reaction step, XRD of secondary product, IR spectra of secondary product has been provided as Table S1, Fig. S1 and Fig. S2. Chemical affinity calculation of closed system has been shown afterwards which has been done in four steps. The calculation is shown in tables from Tables S2 -S8. Table S9-10 shows a calculation of Li incorporation in Mg-clay and its effect on concentration in the reacting solution. pH measured during reaction has been plotted against time and graph is shown as Gig. S3. Further formulas has been shown which are used to calculate CDR potential if precipitation is ignored.

Data Availability:

Data are available through Mendeley Data at: https://doi.org/10.17632/k4frv6ss3v.1

References

Aagaard, P., & Helgeson, H. C. (1982). Thermodynamic and kinetic constraints on reaction rates among minerals and aqueous solutions; I, Theoretical considerations. *American journal of Science, 282*(3), 237-285.

Advocat, T., Chouchan, J. L., Crovisier, J. L., Guy, C., Daux, V., Jegou, C., ... & Vernaz, E. (1997). Borosilicate nuclear waste glass alteration kinetics: chemical inhibition and affinity control. *MRS Online Proceedings Library (OPL)*, 506, 63.

Alekseyev, V. A., Medvedeva, L. S., Prisyagina, N. I., Meshalkin, S. S., & Balabin, A. I. (1997). Change in the dissolution rates of alkali feldspars as a result of secondary mineral

642   precipitation and approach to equilibrium. *Geochimica et Cosmochimica Acta, 61*(6),
643   1125-1142.

644 Angeli, F., Gaillard, M., Jollivet, P., & Charpentier, T. (2006). Influence of glass composition
645   and alteration solution on leached silicate glass structure: a solid-state NMR
646   investigation. *Geochimica et Cosmochimica Acta, 70*(10), 2577-2590.

647

648 Banfield, J. F., Jones, B. F., & Veblen, D. R. (1991). An AEM-TEM study of weathering and
649   diagenesis, Abert Lake, Oregon: II. Diagenetic modification of the sedimentary
650   assemblage. *Geochimica et Cosmochimica Acta, 55*(10), 2795-2810.

651

652 Bas, M. L., Maitre, R. L., Streckeisen, A., Zanettin, B., & IUGS Subcommission on the
653   Systematics of Igneous Rocks. (1986). A chemical classification of volcanic rocks
654   based on the total alkali-silica diagram. *Journal of petrology, 27*(3), 745-750.

655

656 Beerling, D. J., Kantzas, E. P., Lomas, M. R., Wade, P., Eufrasio, R. M., Renforth, P., ... &
657   Banwart, S. A. (2020). Potential for large-scale CO2 removal via enhanced rock
658   weathering with croplands. *Nature*, 583(7815), 242-248.

659

660 Beerling, D. J., Epihov, D. Z., Kantola, I. B., Masters, M. D., Reershemius, T., Planavsky, N.
661   J., ... & Banwart, S. A. (2024). Enhanced weathering in the US Corn Belt delivers
662   carbon removal with agronomic benefits. *Proceedings of the National Academy of*
663   *Sciences*, *121*(9), e2319436121.

664

665 Berger, G., Claparols, C., Guy, C., & Daux, V. (1994). Dissolution rate of a basalt glass in
666   silica-rich solutions: implications for long-term alteration. *Geochimica et*
667   *Cosmochimica Acta, 58*(22), *4875-4886*.

668

669 Berger, G., Schott, J., & Guy, C. (1988). Behaviour of Li, Rb and Cs during basalt glass and
670   olivine dissolution and chlorite, smectite and zeolite precipitation from seawater:
671   experimental investigations and modelisation between 50 and 300° C. *Chemical*
672   *Geology, 71*(4), 297-312.

673

674 Berger, G., Schott, J., & Loubet, M. (1987). Fundamental processes controlling the first stage
675   of alteration of a basalt glass by seawater: an experimental study between 200 and 320°
676   C. *Earth and Planetary Science Letters, 84*(4), 431-445.

677

678 Berner, R. A. (1978). Rate control of mineral dissolution under earth surface
679   conditions. *American Journal of Science, 278*(9), 1235-1252.

680

681 Bettison-Varga, L., & Mackinnon, I. D. (1997). The role of randomly mixed-layered
682   chlorite/smectite in the transformation of smectite to chlorite. *Clays and Clay
683   Minerals, 45*, 506-516.

684

685 Bouakkaz, R., Abdelouas, A., El Mendili, Y., Grambow, B., & Gin, S. (2016). SON68 glass
686   alteration under Si-rich solutions at low temperature (35–90° C): kinetics, secondary
687   phases and isotopic exchange studies. *Rsc Advances, 6*(76), 72616-72633.

688

689 Bourcier, W. L., Ebert, W. L., & Feng, X. (1992). Modelling surface area to volume effects on
690   borosilicate glass dissolution. *MRS Online Proceedings Library (OPL), 294*, 577.

691

692 Brown, K. (2011, May). Thermodynamics and kinetics of silica scaling. In *International
693   Workshop on Mineral Scaling* (p. 8). Manila, Philippines.

694

695 Chakoumakos, B. C., Loong, C. K., & Schultz, A. J. (1997). Low-temperature structure and
696   dynamics of brucite. *The Journal of Physical Chemistry B*, *101*(46), 9458-9462.

697

698 Christidis, G. E. (2006). Genesis and compositional heterogeneity of smectites. Part III:
699   Alteration of basic pyroclastic rocks—A case study from the Troodos Ophiolite
700   Complex, Cyprus. *American Mineralogist, 91*(4), 685-701.

701

702 Crovisier, J. L., Honnorez, J., & Eberhart, J. P. (1987). Dissolution of basaltic glass in seawater:
703   Mechanism and rate. *Geochimica et Cosmochimica Acta*, *51*(11), 2977-2990.

704

Crovisier, J. L., Advocat, T., Petit, J. C., & Fritz, B. (1988a). Alteration of basaltic glass in Iceland as a natural analogue for nuclear waste glasses: geochemical modelling with DISSOL. *MRS Online Proceedings Library (OPL)*, *127*, 57.

Crovisier, J. L., Atassi, H., Daux, V., Honnorez, J., Petit, J. C., & Eberhart, J. P. (1988b). A new insight into the nature of the leached layers formed on basaltic glasses in relation to the choice of constraints for long term modelling. *MRS Online Proceedings Library (OPL)*, *127*, 41.

Crovisier, J. L., & Daux, V. (1990). Populations of clays formed by alteration of subglacial hyaloclastites from Iceland. *Chemical Geology, 84*(1-4), 261-263.

Crovisier, J. L., Advocat, T., & Dussossoy, J. L. (2003). Nature and role of natural alteration gels formed on the surface of ancient volcanic glasses (Natural analogs of waste containment glasses). *Journal of Nuclear Materials, 321*(1), 91-109.

Crovisier, J. L., Honnorez, J., Fritz, B., & Petit, J. C. (1992). Dissolution of subglacial volcanic glasses from Iceland: laboratory study and modelling. *Applied Geochemistry, 7*, 55-81.

Cuadros, J., Afsin, B., Jadubansa, P., Ardakani, M., Ascaso, C., & Wierzchos, J. (2013). Microbial and inorganic control on the composition of clay from volcanic glass alteration experiments. *American Mineralogist*, *98*(2-3), 319-334.

Curti, E., Crovisier, J. L., Morvan, G., & Karpoff, A. M. (2006). Long-term corrosion of two nuclear waste reference glasses (MW and SON68): A kinetic and mineral alteration study. *Applied Geochemistry, 21*(7), 1152-1168.

Daux, V., Crovisier, J. L., Hemond, C., & Petit, J. C. (1994). Geochemical evolution of basaltic rocks subjected to weathering: fate of the major elements, rare earth elements, and thorium. *Geochimica et Cosmochimica Acta, 58*(22), *4941-4954*.

736 Daux, V., Guy, C., Advocat, T., Crovisier, J. L., & Stille, P. (1997). Kinetic aspects of basaltic
737   glass dissolution at 90° C: role of aqueous silicon and aluminium. *Chemical*
738   *Geology, 142*(1-2), 109-126.
739

740 De La Fuente, S., Cuadros, J., Fiore, S., & Linares, J. (2000). Electron microscopy study of
741   volcanic tuff alteration to illite-smectite under hydrothermal conditions. *Clays and Clay*
742   *Minerals, 48*(3), 339-350.
743

744 Decarreau, A., Vigier, N., Pálková, H., Petit, S., Vieillard, P., & Fontaine, C. (2012).
745   Partitioning of lithium between smectite and solution: An experimental
746   approach. *Geochimica et Cosmochimica Acta*, *85*, 314-325.
747

748 Declercq, J., Diedrich, T., Perrot, M., Gislason, S. R., & Oelkers, E. H. (2013). Experimental
749   determination of rhyolitic glass dissolution rates at 40–200° C and 2< pH<
750   10.1. *Geochimica et Cosmochimica Acta*, *100*, 251-263.
751

752 Dehouck, E., McLennan, S. M., Meslin, P. Y., & Cousin, A. (2014). Constraints on abundance,
753   composition, and nature of X-ray amorphous components of soils and rocks at Gale
754   crater, Mars. *Journal of Geophysical Research: Planets, 119*(12), 2640-2657.
755

756 Dessert, C., Dupré, B., François, L. M., Schott, J., Gaillardet, J., Chakrapani, G., & Bajpai, S.
757   (2001). Erosion of Deccan Traps determined by river geochemistry: impact on the
758   global climate and the $^{87}Sr/^{86}Sr$ ratio of seawater. *Earth and Planetary Science*
759   *Letters, 188*(3-4), 459-474.
760 Dessert, C., Dupré, B., Gaillardet, J., François, L. M., & Allègre, C. J. (2003). Basalt
761   weathering laws and the impact of basalt weathering on the global carbon cycle.
762   *Chemical Geology, 202*(3-4), 257-273.
763

764 Eggleton, R. A., Foudoulis, C., & Varkevisser, D. (1987). Weathering of basalt: changes in rock
765   chemistry and mineralogy. *Clays and Clay Minerals, 35*, 161-169.
766

767 Fang, Q., Lu, A., Hong, H., Kuzyakov, Y., Algeo, T. J., Zhao, L., ... & Chorover, J. (2023).
768   Mineral weathering is linked to microbial priming in the critical zone. *Nature*
769   *Communications, 14*(1), 345.
770

771 Fiore, S., Huertas, F. J., Huertas, F., & Linares, J. (2001). Smectite formation in rhyolitic
772   obsidian as inferred by microscopic (SEM-TEM-AEM) investigation. *Clay*
773   *Minerals*, *36*(4), 489-500.
774

775 Fox, L. E. (1988). The solubility of colloidal ferric hydroxide and its relevance to iron
776   concentrations in river water. *Geochimica et Cosmochimica Acta, 52*(3), 771-777.
777

778 Frings, P. J., & Buss, H. L. (2019). The central role of weathering in the geosciences. *Elements:*
779   *An International Magazine of Mineralogy, Geochemistry, and Petrology*, *15*(4), 229-
780   234.
781

782 Ghiara, M. R., Franco, E., Petti, C., Stanzione, D., & Valentino, G. M. (1993). Hydrothermal
783   interaction between basaltic glass, deionized water and seawater. *Chemical*
784   *Geology*, *104*(1-4), 125-138.
785

786 Gin, S., Ryan, J. V., Schreiber, D. K., Neeway, J., & Cabié, M. (2013). Contribution of atom-
787   probe tomography to a better understanding of glass alteration mechanisms:
788   Application to a nuclear glass specimen altered 25 years in a granitic
789   environment. *Chemical Geology, 349*, 99-109.
790

791 Gislason, S. R., & Arnórsson, S. (1993). Dissolution of primary basaltic minerals in natural
792   waters: saturation state and kinetics. *Chemical Geology*, *105*(1-3), 117-135.
793

794 Gislason, S. R., & Eugster, H. P. (1987a). Meteoric water-basalt interactions. I: A laboratory
795   study. *Geochimica et Cosmochimica Acta*, *51*(10), 2827-2840.
796

797 Gislason, S. R., & Eugster, H. P. (1987b). Meteoric water-basalt interactions. II: A field study
798   in NE Iceland. *Geochimica et Cosmochimica Acta, 51*(10), *2841-2855*.
799

800 Gislason, S. R., & Oelkers, E. H. (2003). Mechanism, rates, and consequences of basaltic glass
801   dissolution: II. An experimental study of the dissolution rates of basaltic glass as a
802   function of pH and temperature. *Geochimica et Cosmochimica Acta*, *67*(20), 3817-
803   3832.
804
805 Goll, D. S., Ciais, P., Amann, T., Buermann, W., Chang, J., Eker, S., ... & Vicca, S. (2021).
806   Potential CO2 removal from enhanced weathering by ecosystem responses to powdered
807   rock. *Nature Geoscience*, *14*(8), 545-549.
808
809 Grambow, B., Jercinovic, M. J., Ewing, R. C., & Byers, C. D. (1985). Weathered basalt glass:
810   a natural analogue for the effects of reaction progress on nuclear waste glass
811   alteration. *MRS Online Proceedings Library (OPL), 50*, 263.
812
813 Guy, C., & Schott, J. (1989). Multisite surface reaction versus transport control during the
814   hydrolysis of a complex oxide. *Chemical Geology, 78*(3-4), 181-204.
815
816 Heřmanská, M., Voigt, M. J., Marieni, C., Declercq, J., & Oelkers, E. H. (2023). A
817   comprehensive and consistent mineral dissolution rate database: part II: secondary
818   silicate minerals. *Chemical Geology, 636*, 121632.
819
820 Keller, W. D., Reynolds, R. C., & Inoue, A. (1986). Morphology of clay minerals in the
821   smectite-to-illite conversion series by scanning electron microscopy. *Clays and Clay*
822   *Minerals, 34*, 187-197.
823
824 Kump, L. R., Brantley, S. L., & Arthur, M. A. (2000). Chemical weathering, atmospheric CO_2,
825   and climate. *Annual Review of Earth and Planetary Sciences, 28*(1), 611-667.
826
827 Lasaga, A. C., Soler, J. M., Ganor, J., Burch, T. E., & Nagy, K. L. (1994). Chemical weathering
828   rate laws and global geochemical cycles. *Geochimica et Cosmochimica Acta, 58*(10),
829   *2361-2386*.
830
831 Leturcq, G., Berger, G., Advocat, T., & Vernaz, E. (1999). Initial and long-term dissolution
832   rates of aluminosilicate glasses enriched with Ti, Zr and Nd. *Chemical Geology, 160*(1-
833   2), 39-62.

834

835 Loock, S., van Wyk de Vries, B., & Hénot, J. M. (2010). Clinker formation in basaltic and
836   trachybasaltic lava flows. *Bulletin of volcanology, 72*, 859-870.

837

838 Meng, J., Liu, X., Li, B., Zhang, J., Hu, D., Chen, J., & Shi, W. (2018). Conversion reactions
839   from dioctahedral smectite to trioctahedral chlorite and their structural
840   simulations. *Applied Clay Science, 158*, 252-263.

841

842 Meunier, A., Petit, S., Cockell, C. S., El Albani, A., & Beaufort, D. (2010). The Fe-rich clay
843   microsystems in basalt-komatiite lavas: importance of Fe-smectites for pre-biotic
844   molecule catalysis during the Hadean eon. *Origins of Life and Evolution of*
845   *Biospheres*, *40*(3), 253-272.

846

847 Murphy, W. M., Oelkers, E. H., & Lichtner, P. C. (1989). Surface reaction versus diffusion
848   control of mineral dissolution and growth rates in geochemical processes. *Chemical*
849   *Geology, 78*(3-4), 357-380.

850

851 Nagy, K. L., & Lasaga, A. C. (1992). Dissolution and precipitation kinetics of gibbsite at 80°
852   C and pH 3: The dependence on solution saturation state. *Geochimica et Cosmochimica*
853   *Acta, 56*(8), *3093-3111*.

854

855 Nagy, K. L., Blum, A. E., & Lasaga, A. C. (1991). Dissolution and precipitation kinetics of
856   kaolinite at 80° C and pH 3; the dependence on solution saturation state. *American*
857   *Journal of Science, 291*(7), 649-686.

858

859 Neeway, J. J., Kerisit, S. N., Liu, J., Zhang, J., Zhu, Z., Riley, B. J., & Ryan, J. V. (2016). Ion-
860   exchange interdiffusion model with potential application to long-term nuclear waste
861   glass performance. *The Journal of Physical Chemistry C, 120*(17), 9374-9384.

862

863 Nesbitt, H. W., & Wilson, R. E. (1992). Recent chemical weathering of basalts. American
864   *Journal of science, 292*(10), 740-777.

865

866 Oelkers, E. H., & Gislason, S. R. (2001). The mechanism, rates and consequences of basaltic
867   glass dissolution: I. An experimental study of the dissolution rates of basaltic glass as a

868   function of aqueous Al, Si and oxalic acid concentration at 25° C and pH= 3 and
869   11. *Geochimica et cosmochimica acta, 65*(21), 3671-3681.
870
871 Parkhurst, D. L., & Appelo, C. A. J. (1999). User's guide to PHREEQC (Version 2): A computer
872   program for speciation, batch-reaction, one-dimensional transport, and inverse
873   geochemical calculations. *Water-resources investigations report, 99*(4259), 312.
874
875 Parruzot, B., Jollivet, P., Rébiscoul, D., & Gin, S. (2015). Long-term alteration of basaltic glass:
876   Mechanisms and rates. *Geochimica et Cosmochimica Acta, 154*, 28-48.
877
878 Paul, A. (1977). Chemical durability of glasses; a thermodynamic approach. *Journal of
879   materials science, 12*, 2246-2268.
880
881 Rinder, T., & von Hagke, C. (2021). The influence of particle size on the potential of enhanced
882   basalt weathering for carbon dioxide removal-Insights from a regional
883   assessment. *Journal of Cleaner Production*, *315*, 128178.
884
885 Rowe, M. C., & Brewer, B. J. (2018). AMORPH: A statistical program for characterizing
886   amorphous materials by X-ray diffraction. *Computers & geosciences, 120*, 21-31.
887
888 Schuiling, R. D., & Krijgsman, P. (2006). Enhanced weathering: an effective and cheap tool to
889   sequester CO_2. *Climatic Change, 74*(1), 349-354.
890
891 Shannon, R. D. (1976). Revised effective ionic radii and systematic studies of interatomic
892   distances in halides and chalcogenides. *Acta crystallographica section A: crystal
893   physics, diffraction, theoretical and general crystallography*, *32*(5), 751-767.
894
895 Spanos, N., & Koutsoukos, P. G. (1998). Kinetics of precipitation of calcium carbonate in
896   alkaline pH at constant supersaturation. Spontaneous and seeded growth. *The Journal
897   of Physical Chemistry B*, *102*(34), 6679-6684.
898

899 Sriwastava, P., Singh, V. V., Mathew, G., Kogure, T., & Myneni, S. (2023). Origin of clays in
900   the interbasaltic red boles of Deccan Volcanics: Pedogenesis versus
901   palagonitization. *Applied Clay Science, 246*, 107183.
902
903 Stefánsson, A., & Gíslason, S. R. (2001). Chemical weathering of basalts, Southwest Iceland:
904   effect of rock crystallinity and secondary minerals on chemical fluxes to the
905   ocean. *American Journal of Science, 301*(6), 513-556.
906
907 Strefler, J., Amann, T., Bauer, N., Kriegler, E., & Hartmann, J. (2018). Potential and costs of
908   carbon dioxide removal by enhanced weathering of rocks. *Environmental Research*
909   *Letters*, *13*(3), 034010.
910
911 Taylor, L. L., Driscoll, C. T., Groffman, P. M., Rau, G. H., Blum, J. D., & Beerling, D. J. (2020).
912   Increased carbon capture by a silicate-treated forested watershed affected by acid
913   deposition. *Biogeosciences Discussions*, *2020*, 1-29.
914
915 Techer, I., Advocat, T., Lancelot, J., & Liotard, J. M. (2001). Dissolution kinetics of basaltic
916   glasses: control by solution chemistry and protective effect of the alteration
917   film. *Chemical Geology, 176*(1-4), 235-263.
918
919 Techner, I., Advocat, T., Vernaz, E., Lancelot, J. R., & Liotard, J. M. (1998). Dissolution rate
920   equations for basaltic glasses. Comparison with experimental data. *Mineral Mag A*, *62*,
921   1498-1499.
922
923 Thorpe, M.T., Bristow, T.F., Rampe, E.B., Tosca, N.J., Grotzinger, J.P., Bennett, K.A., Achilles,
924   C.N., Blake, D.F., Chipera S.J., Downs, G., Downs, R.T., Morrison, S.M., Tu, V., Castle,
925   N., Craig, P., Marais, D.J.D., Hazen, R.M., Ming, D.W., Morris, R.V., Treiman, A.H.,
926   Vaniman, D.T., Yen, A.S., Vasavada, A.R., Dehouck, E., Bridges, J.C., Berger, J.,
927   McAdam, A., Peretyazhko, T., Siebach, K.L., Bryk, A.B., Fox, V.K., & Fedo, C.M.
928   (2022) Mars Science Laboratory CheMin data from the Glen Torridon region and the
929   significance of lake-groundwater interactions in interpreting mineralogy and
930   sedimentary history. *Journal of Geophysical research: Planets, 127*(11),
931   e2021JE007099

Toner, J. D., & Catling, D. C. (2019). Alkaline lake settings for concentrated prebiotic cyanide and the origin of life. *Geochimica et Cosmochimica Acta, 260,* 124-132.

Toner, J. D., & Catling, D. C. (2020). A carbonate-rich lake solution to the phosphate problem of the origin of life. *Proceedings of the National Academy of Sciences, 117*(2), 883-888.

Treiman, A.H., Bish, D.L., Vaniman, D.T., Chipera, S.J., Blake, D.F., Ming, D.W., Morris, R.V., Bristow, T.F., Morrison, S.M., Baker, M.B., Rampe, E.B., Downs, R.T., Filiberto, J., Glazner, A.F., Gellert, R., Thompson, L.M., Schmidt, M.E., Deit, L.L., Weins, R.C., McAdam, A.C., Achilles, C.N., Edgett, K.S., Farmer, J.D., Fendrich, K.V., Grotzinger, J.P., Gupta, S., Morookian, J.M., Newcomb, M.E., Rice, M.S., Spray, J.G., Stolper, E.M., Sumner, D.Y., Vaavada, A.R., & Yen, A.S. (2016). Mineralogy, provenance, and diagenesis of a potassic basaltic sandstone on Mars: ChemMin X-rat diffraction of the Windjana sample (Kimberley area, Gale Crater). *Journal of geophysics Research: Planets, 121*(1), 75-106

Tsipursky, S. I., & Drits, V. A. (1984). The distribution of octahedral cations in the 2: 1 layers of dioctahedral smectites studied by oblique-texture electron diffraction. *Clay minerals*, *19*(2), 177-193.

Velde, B. B., & Meunier, A. (2008). The origin of clay minerals in soils and weathered rocks. *Springer Science & Business Media*.

Vernaz, E., Gin, S., Jégou, C., & Ribet, I. (2001). Present understanding of R7T7 glass alteration kinetics and their impact on long-term behavior modeling. *Journal of Nuclear Materials, 298*(1-2), 27-36.

Vienne, A., Poblador, S., Portillo-Estrada, M., Hartmann, J., Ijiehon, S., Wade, P., & Vicca, S. (2022). Enhanced weathering using basalt rock powder: carbon sequestration, co-benefits and risks in a mesocosm study with Solanum tuberosum. *Frontiers in Climate*, *4*, 869456.

Wojdyr, M. (2010). Fityk: a general-purpose peak fitting program. *Journal of applied crystallography, 43*(5), 1126-1128.

966 Wolff-Boenisch, D., Gislason, S. R., Oelkers, E. H., & Putnis, C. V. (2004). The dissolution
967   rates of natural glasses as a function of their composition at pH 4 and 10.6, and
968   temperatures from 25 to 74 C. *Geochimica et Cosmochimica Acta*, *68*(23), 4843-4858.

969 Zhu, C., Blum, A. E., & Veblen, D. R. (2004). Feldspar dissolution rates and clay precipitation
970   in the Navajo aquifer at Black Mesa, Arizona, USA. *Water-rock interaction*, *11*, 895-
971   899.

972 Zhu, C., & Lu, P. (2009). Alkali feldspar dissolution and secondary mineral precipitation in
973   batch systems: 3. Saturation states of product minerals and reaction paths. *Geochimica*
974   *et Cosmochimica Acta*, *73*(11), 3171-3200.

975

976 Zhu, C., Lu, P., Zheng, Z., & Ganor, J. (2010). Coupled alkali feldspar dissolution and
977   secondary mineral precipitation in batch systems: 4. Numerical modeling of kinetic
978   reaction paths. *Geochimica et Cosmochimica Acta*, *74*(14), 3963-3983.

979

List of Figures

evolution with time. The blue dot indicates the ratio in reacting solution, while the orange dot indicates the constant value in basalt glass.

Fig-6 Normalised mass loss plot ~~with respect~~ to time. ~~B~~The blue diamond indicates the experiment with <36 μm fraction of basalt glass. The orange square indicates an experiment with a 36-56 μm fraction of basalt glass.

Fig-7 Saturation index versus time for reaction setup with grain size (36-56 μm). Solid lines show minerals that reach~~es~~ the oversaturation state during the reaction; the colours are specific to the mineral variety. Coloured bands in the background of the image mark the zone of oversaturation of the specific mineral mentioned within the coloured band.

Fig-8 Variation of total reaction affinity (ΔG_r) with dissolution rate (r) corresponding to each step of reaction. The dotted blue line indicates the expected theoretical trend between total reaction affinity and rate, according to transition state theory (TST). The orange diamond indicates an experiment with a 36-56 μm fraction of glass, and the blue circle indicates an experiment with <36 μm glass. The greenish band showed the experimental data when reaction affinity was calculated according to the consideration in Techer et al. (2001), which results in a shift in ΔG_r in the negative direction. The yellow band shows the experimental points data when total reaction affinity was calculated considering brucite in equilibrium with the reacting solution and basalt.

Fig-9 Amount of bivalent cations (Ca+Mg) in fluid interacting with basalt glass in a closed system. Measured values are sum of the concentrations of Ca and Mg at each reaction step. ~~C~~The calculated amount of bivalent cations ~~are resulted~~results when secondary precipitation is not considered, and total cation~~s~~ released from basalt are estimated from a normalised mass loss rate. The calculated values automatically incorporate~~s~~ effect of precipitation on rates of dissolution in closed system.

List of tables

Table-1 Experimental setup

Setup no.	Rock: water ratio	temperature	Grain size	Surface area
1	1:100	90 °C	36–56 μm	4.51 ± 0.01 m^2/g
2	1:100	90 °C	<36 μm	6.38 ± 0.33 m^2/g

Table-2 Glass composition

Element/Oxide	EPMA of 25 grains (Anhydrous basis)		ICP AES (Anhydrous basis)	ICP-MS
	Average (%)	dev	Bulk chemistry (%)	(ppm)
Na_2O	2.46	0.043	2.25	-
MgO	6.47	0.082	7.56	-
Al_2O_3	13.6	0.068	12.6	-
SiO_2	51.9	0.466	50.57	-
P_2O_5	0.25	0.026	0.22	-
K_2O	0.37	0.025	0.36	-
CaO	9.92	0.133	11.47	-
TiO_2	2.25	0.068	2.5	-
MnO	0.17	0.027	0.17	-
Fe_2O_3	12.5	0.17	12.32	-
Li	-	-	-	5.27

Table-3 Elemental Composition evolution in both experimental setup (<36 μm and 36–56 μm)

time (hrs)	pH	Reaction setup with < 36 μm grain size							Normalised mass loss (g/m²)	Reaction setup with 36-56 μm grain size							Normalised mass loss (g/m²)
		concentrations								concentrations							
		Si (ppm)	Al (ppm)	Na (ppm)	Ca (ppm)	K (ppm)	Mg (ppm)	Li (ppb)		Si (ppm)	Al (ppm)	Na (ppm)	Ca (ppm)	K (ppm)	Mg (ppm)	Li (ppb)	
2	8.7	7.11	0.77	11.32	1.13	0.89	0.73	1.34	-	1.31	0.38	15.14	0.5	29.04	0.09	0.94	19.79
4		9.02	0.88	7.28	1.77	0.79	1.12	0.51	7.56	2.35	0.36	6.43	0.95	11.66	0.35	0.44	9.22
6		10.02	0.49	8.56	2.19	0.85	1.29	3.33	-	4.41	0.37	6.79	1.29	11.59	0.41	0.82	17.12
8		10.87	0.73	6.51	2.39	0.78	1.33	0.71	10.43	6.11	0.33	7.11	1.51	12.15	0.71	1.46	30.35
10		14.54	0.95	24.37	0.37	0.64	bdl	0.84	12.29	7.24	0.49	6.93	1.69	11.96	0.83	0.39	8.07
12		11.28	0.51	7.27	2.51	0.74	1.38	2.96	-	8.49	0.64	7.4	1.79	12.13	0.96	1.67	34.43
14		12.29	1.61	6.72	2.73	0.92	1.36	0.55	7.98	9.29	0.68	7.02	2.37	11.78	1.11	0.47	9.65
16		12.7	1.48	6.12	2.89	0.66	1.43	0.46	6.65	9.3	0.5	7.03	2.13	11.96	1.06	0.59	12.06
18	9	13.67	2.13	6.1	3.21	1.49	1.53	0.61	8.78	13.32	1.98	6.12	3.15	1.54	1.44	0.66	13.43
20		17.23	1.4	11.42	5.98	3.7	1.75	0.5	7.16	14.25	1.34	13.76	5.33	27.83	1.67	0.8	16.21
22		20.01	1.31	11.56	6.28	3.53	1.77	0.59	8.41	17.09	1.56	13.69	5.1	27.67	1.71	0.6	12.11
24		23.13	2.21	11.65	6.47	3.43	1.68	0.61	8.66	21.98	1.9	14.11	5.59	28.39	1.69	0.73	14.66
28		24.18	1.57	13.62	7.16	4.73	1.69	0.78	11.03	21.71	1.68	12.97	6.26	26.4	1.7	0.86	17.2
32		23.13	1.72	13.83	6.85	27.65	1.91	0.65	9.15	23.4	2.1	12.12	7.28	3.45	1.68	0.89	17.72
36		25.77	2.02	12.27	7.3	3.73	1.62	0.77	10.79	25.16	1.33	16.26	6.47	31.09	1.79	1.44	28.55
40		28.82	2.08	12.4	7.1	3.78	1.59	0.83	11.58	27.51	2	14.76	6.08	29.33	1.71	0.61	12.04
44		32.36	2.07	12.86	7.75	4.01	1.52	0.75	10.42	28.3	1.57	14.23	6.64	28.57	1.69	0.81	15.92
48	9.3	32.4	1.5	13.76	8.09	4.2	1.46	0.98	13.55	31.96	2.68	14.85	7.32	29.34	1.83	1.19	23.28
54		33.59	2.91	13.47	8.83	4.39	1.38	1.69	23.26	28.99	2.79	15.44	8.3	32.34	1.95	1.14	22.2
60		16.42	1.61	7.62	3.84	2.26	0.94	1.26	17.27	15.71	1.44	8.96	3.33	19.31	1.4	0.78	15.12
66		17.33	1.13	7.95	4.07	2.12	0.83	1.2	16.37	14.78	1.31	9.1	3.13	19.07	1.24	0.82	15.82
72		16.94	1.25	7.59	4.12	2.34	0.67	1.44	19.56	16.8	1.39	9.31	3.48	19.74	1.12	1.93	37.08
78	9.37	18.55	1.25	8.17	4.54	8.6	0.68	1.38	18.65	16.89	1.4	9.05	3.64	20.49	1.07	1.78	34.04
84		18.73	1.3	8.22	4.5	8.65	0.69	1.89	25.43	17.71	1.57	10.05	3.97	21.66	1.11	1.26	23.98
90		19.42	1.16	8.61	4.37	9.03	0.48	1.8	24.11	17.94	1.88	9.81	3.55	21.42	0.84	1.57	29.75
96		20.09	1.25	8.47	4.59	8.81	0.45	1.28	17.06	18.76	1.57	10.39	3.82	22.62	0.92	1.58	29.8

| 102		31.52	1.01	10.07	5.77	9.94	0.48	1.43	18.98	26.49	1.3	10.82	4.47	24.44	0.87	1.57	29.47
108		27.71	1.01	9.63	5.39	9.41	0.39	1.65	21.79	24.22	1.14	10.86	4.4	23.9	0.7	1.42	26.53
114		27.1	1.55	9.3	5.57	9.3	0.24	-	-	21.32	0.93	10.53	3.84	22.68	0.56	1.48	27.52
120		25.42	0.95	9.9	5.33	9.71	0.28	1.31	17.14	21.55	0.91	10.75	4.4	22.99	0.51	1.8	33.32
126	9.3	23.78	0.85	9.43	5.33	12.04	0.17	1.88	24.48	20.94	1.18	9.89	4.1	22.17	0.44	1.6	29.47
132		25.04	1.05	9.62	5.26	12.32	0.17	1.38	17.88	26.1	0.97	12.25	4.6	26.85	0.52	1.34	24.57
138		25.55	1.01	10.73	6.32	13.59	0.33	1.42	18.32	22.93	0.93	11.76	4.6	25.43	0.55	1.33	24.27
144		26.06	1.3	10.3	5.72	13.44	0.07	1.57	20.15	22.32	0.94	11.93	4.48	25.68	0.47	2.16	39.22
150		24.49	1.05	10.27	5.32	12.93	0.02	1.62	20.69	21.61	1.19	11.01	4.16	23.89	0.33	1.28	23.13
164		26.24	0.91	11.24	5.58	13.84	bdl	1.81	23.01	22.13	0.86	11.28	4.1	24.19	0.14	1.45	26.07
188	9.35	25.83	0.58	11.38	5.19	13.74	bdl	1.99	25.17	23.01	0.75	12.23	4.59	25.71	0.26	2.35	42.05
212	9.35	28.31	0.81	11.88	5.87	14.21	bdl	2.18	27.44	23.75	0.8	12.28	4.37	25.6	0.1	2.12	37.75
236		30.67	0.96	12.48	5.58	15.17	bdl	2.1	26.30	27.95	1.42	13.03	4.63	26.81	bdl	2.72	48.2
260		33.15	1.21	12.73	6.27	15.51	bdl	1.95	24.30	30.15	0.64	14.5	4.58	29.2	bdl	2.07	36.5
284	9.41	35.08	0.45	14.14	5.84	16.54	bdl	2.31	28.65	28.43	0.37	14.7	4.38	31.01	bdl	2.26	39.65
308		36.92	0.4	14.85	5.85	17.37	bdl	2.45	30.23	36.94	1.02	17.17	2.66	32.77	bdl	2.14	37.36
332	8.85	37.3	0.61	16.08	2.16	16.82	bdl	2.2	27.01	37.1	0.97	17.98	1.88	34.23	bdl	1.7	29.53
356		38.3	0.71	14.35	2.73	16.31	bdl	2.1	25.65	38.79	0.98	17.09	3.2	36.72	bdl	2.97	51.32
404	8.85	43.56	0.6	17.19	3.27	18.35	bdl	3.86	-	41.43	0.69	19.15	2.71	37.28	bdl	7.45	-
452	8.85	50.05	0.56	19.93	4.55	19.89	bdl	-		46.93	0.6	21.54	2.16	41.39	bdl	3.15	53.88
548	8.6	59.07	0.46	22.69	8.74	23.08	bdl	4.03	-	54.73	0.47	23.17	6.63	45.97	bdl	3.92	66.71

bdl= below detection limit

**Table-4 Chemical composition of secondary products formed in both set up of experiments**

| Element Wt %	Secondary products in <36 µm grains experiment								Secondary product in 36–56 µm grains experiment										
	Honey comb shape				Ellipsoid shape		Equant phase		Honey comb shape				Equant aggregate			Equant phase			
Si	23.49	23.05	25.49	23.8	23.82	25.82	24.13	26.02	24.05	25.56	24.68	21.95	26.23	27.17	10.47	6.84	8.98	6.55	11.19
Al	8.02	7.49	7.16	7.02	10.23	9.88	7.92	8.85	6.06	8.95	1.55	4.51	2.84	4.08	3.27	3.18	2.78	2.3	2.42
Na	1.46	1.74	1.82	1.87	0.4	0	0.52	1.16	0.45	0.09	0.69	0.97	0.47	1.45	0.41	1.74	0.01	2.63	0
Mg	4.46	4.3	4.16	4.87	1.43	1.13	0.56	1.78	3.88	3.4	3.01	3.81	0.6	2.55	1.46	0.39	1.92	0.27	0
K	0.35	0.28	0.37	0.62	1.25	1.07	0.44	0.6	0.83	0	0.88	0.47	0.92	0.82	1.16	0	0	0.49	0.25
Ca	6.8	6.36	7.73	6.24	6.66	5.5	6.96	5.31	9.62	13.25	13.85	11.22	4.72	7.49	7.93	10.12	9.13	10.47	12
Fe	7.66	8.87	11.95	8.93	3.55	4.85	4.85	1.99	17.94	20.24	21.54	18.31	27.85	15.46	44.19	48.18	48.58	36.28	42.71
Mn	0.74	0.34	0	0	0.48	0	0	0	1.22	0.15	0	1.29	0	0.75	0	1.53	0	1.62	1.6
O	45.57	46.02	39.43	44.99	51.45	51.74	54.6	54.13	31.96	24.14	21.95	30.71	36.2	37	27.65	24.81	25.71	35.61	25.6
Ti	1.44	1.55	1.89	1.66	0.72	0	0	0.15	3.6	4.21	3.24	2.41	0.17	3.24	3.46	3.22	2.88	3.78	4.24
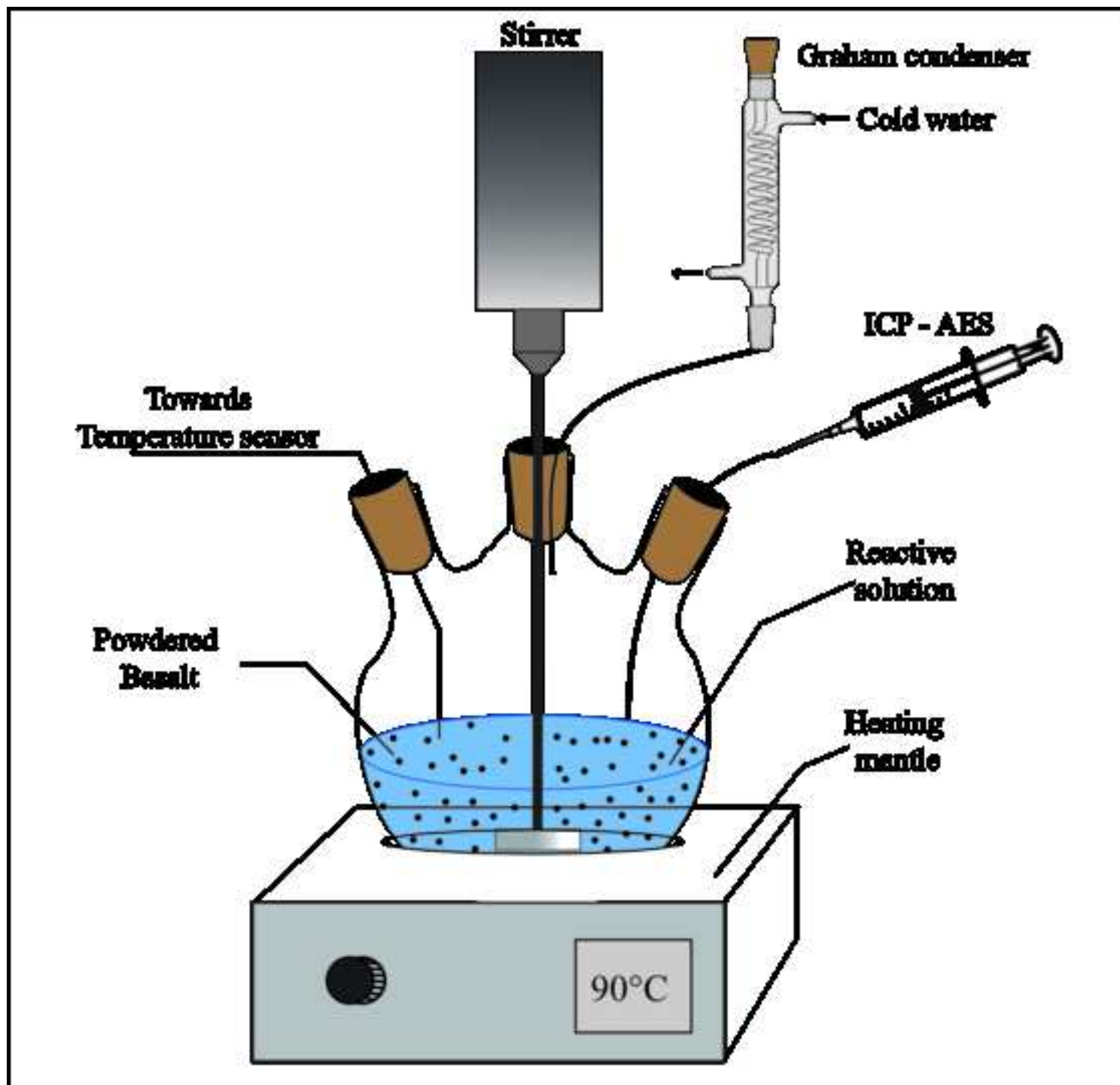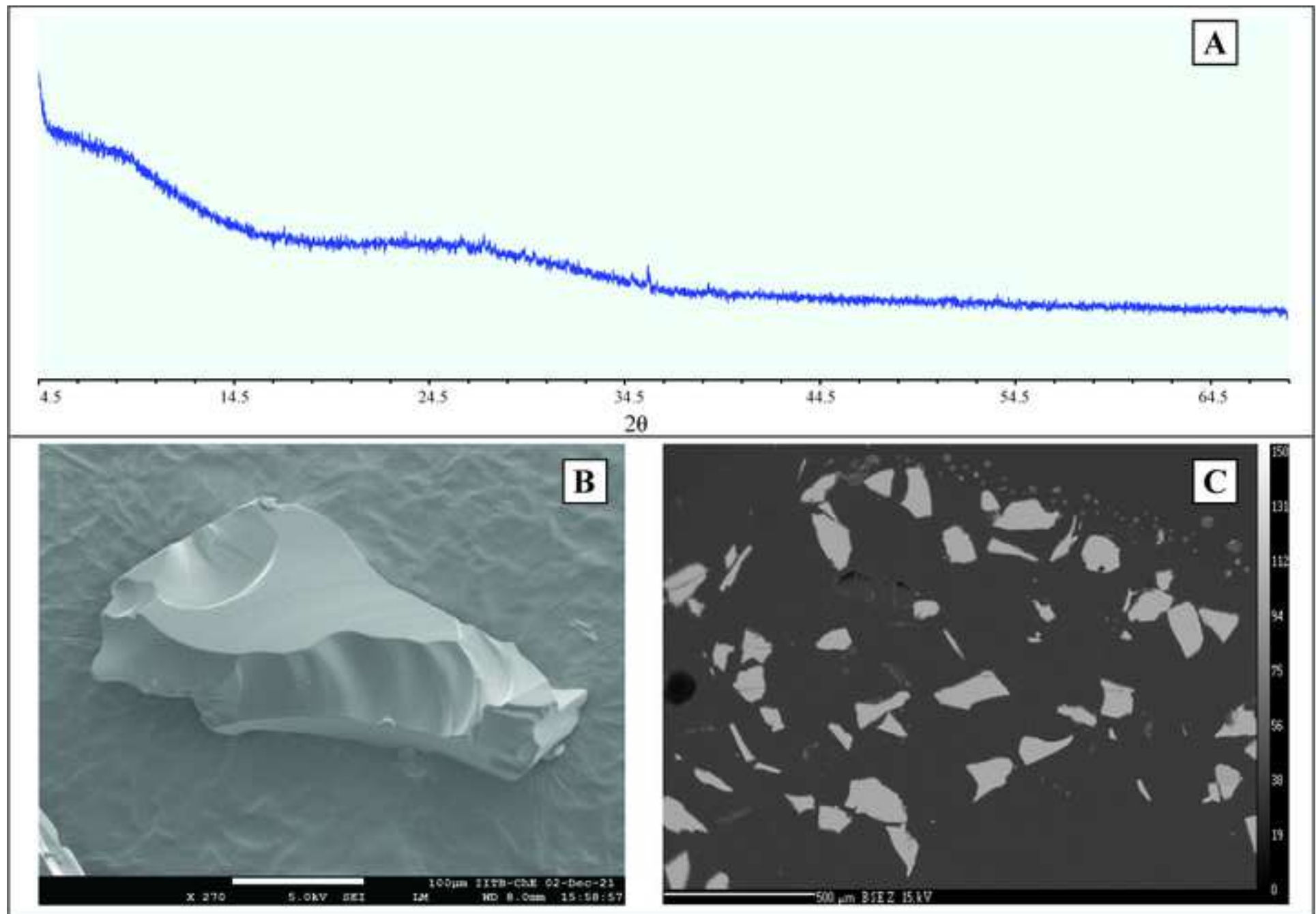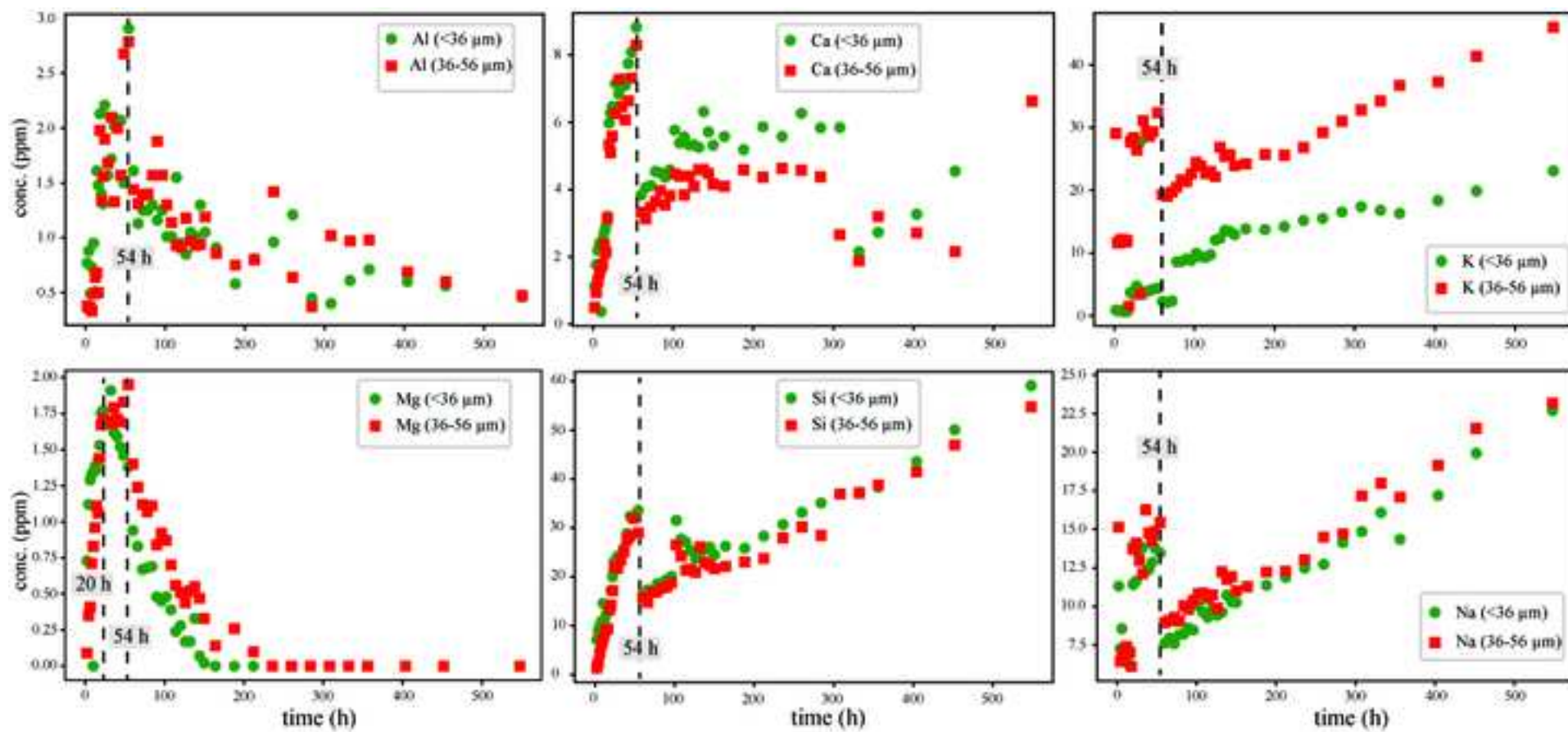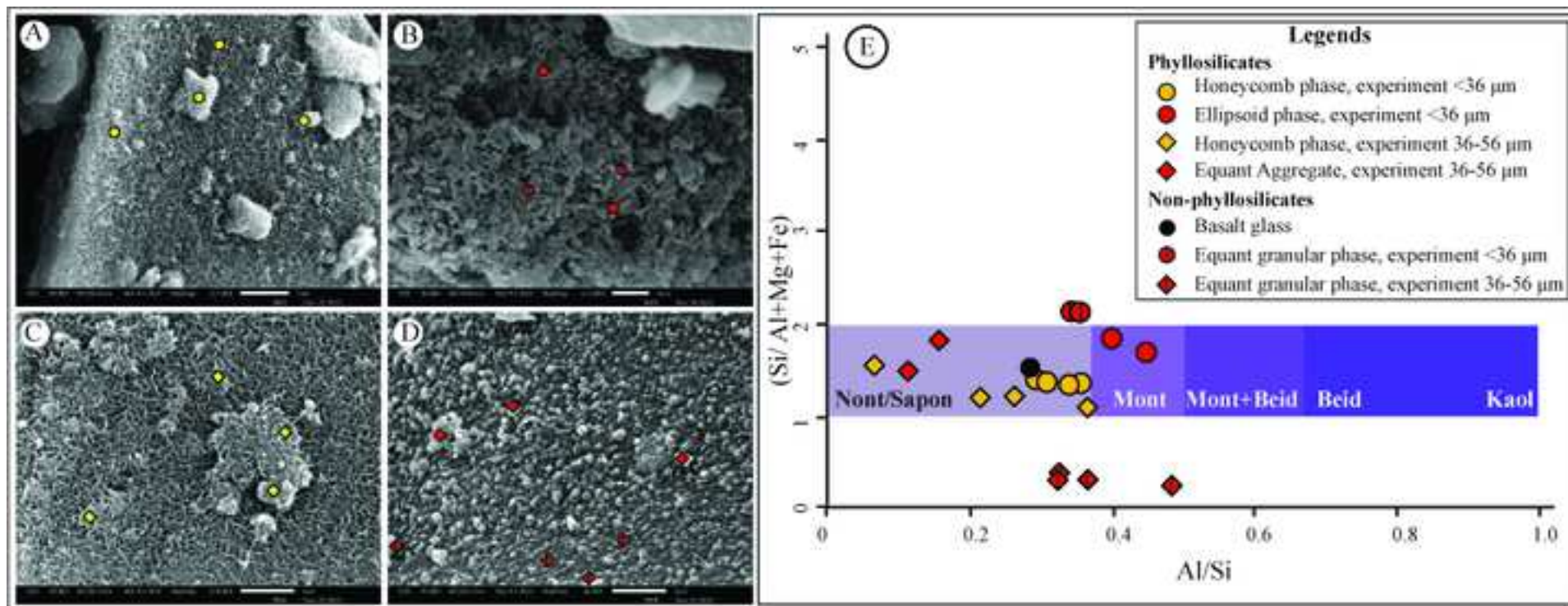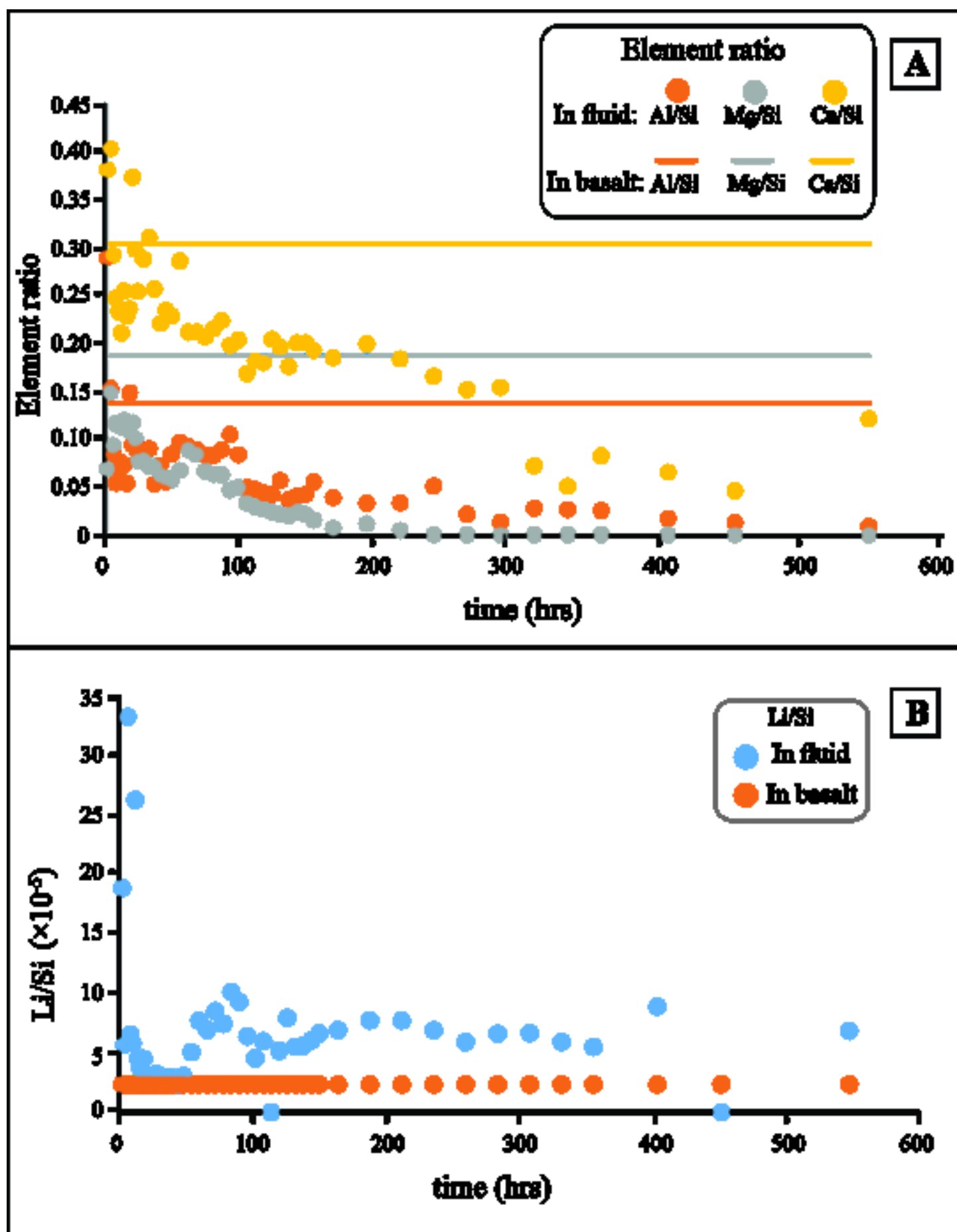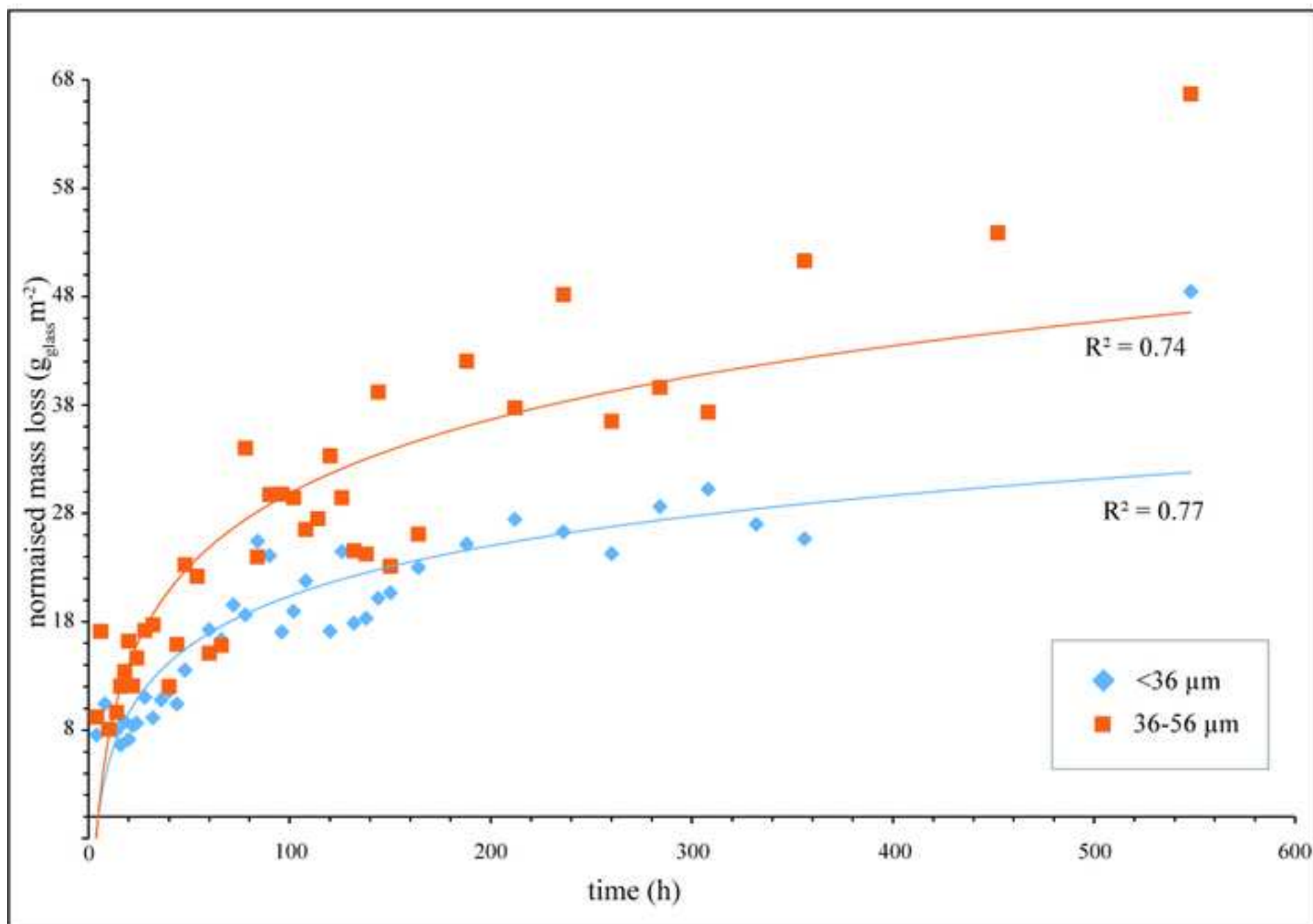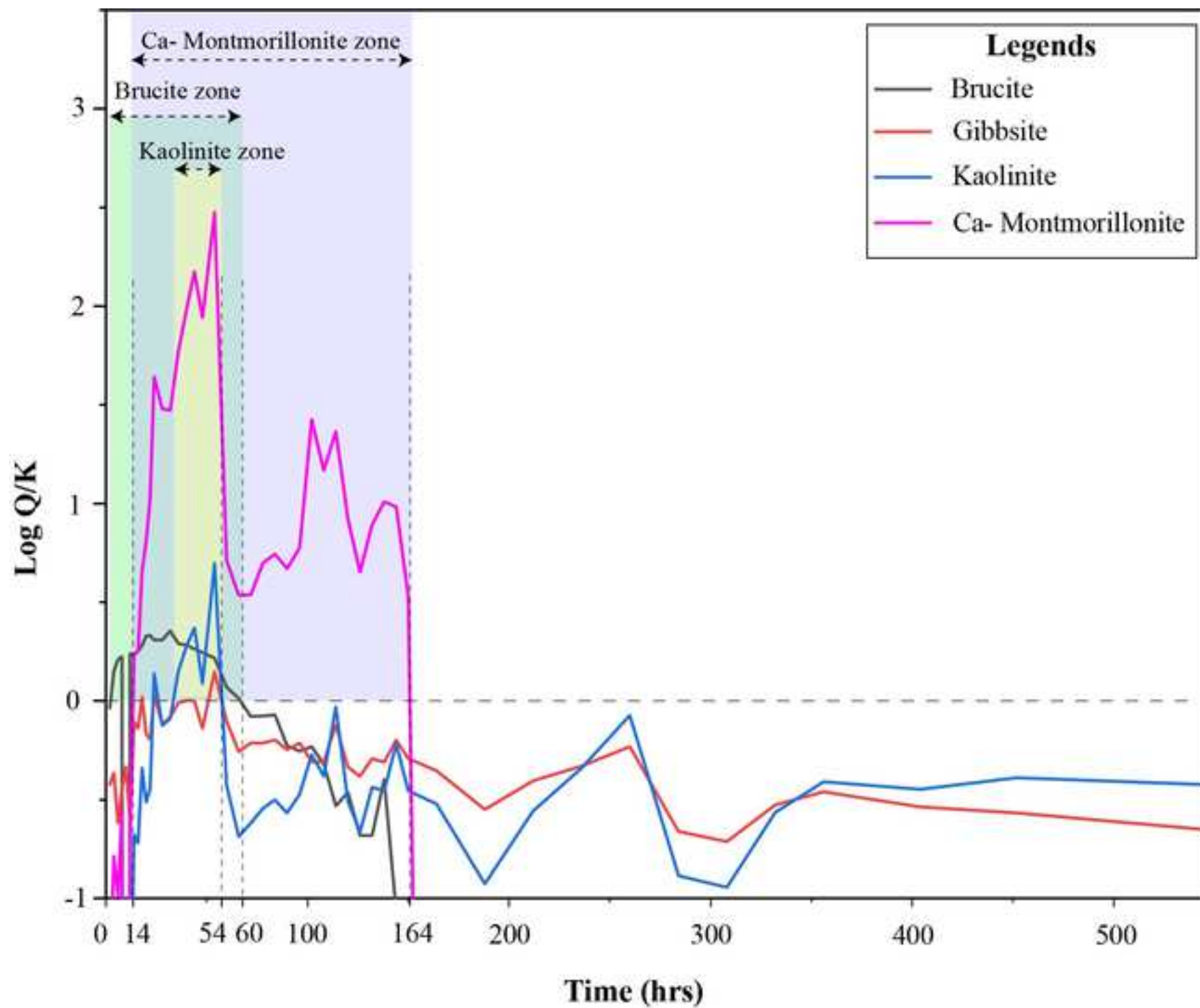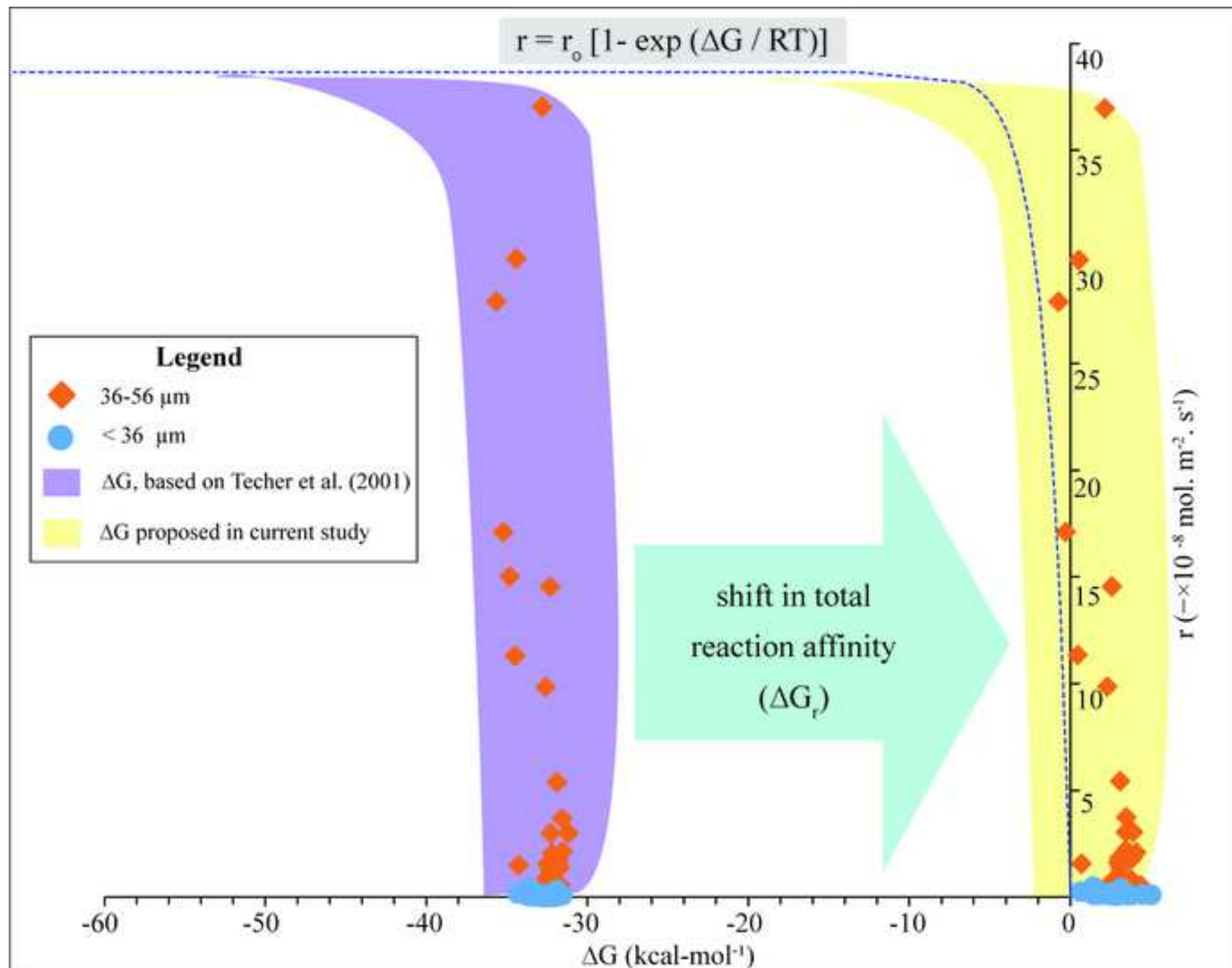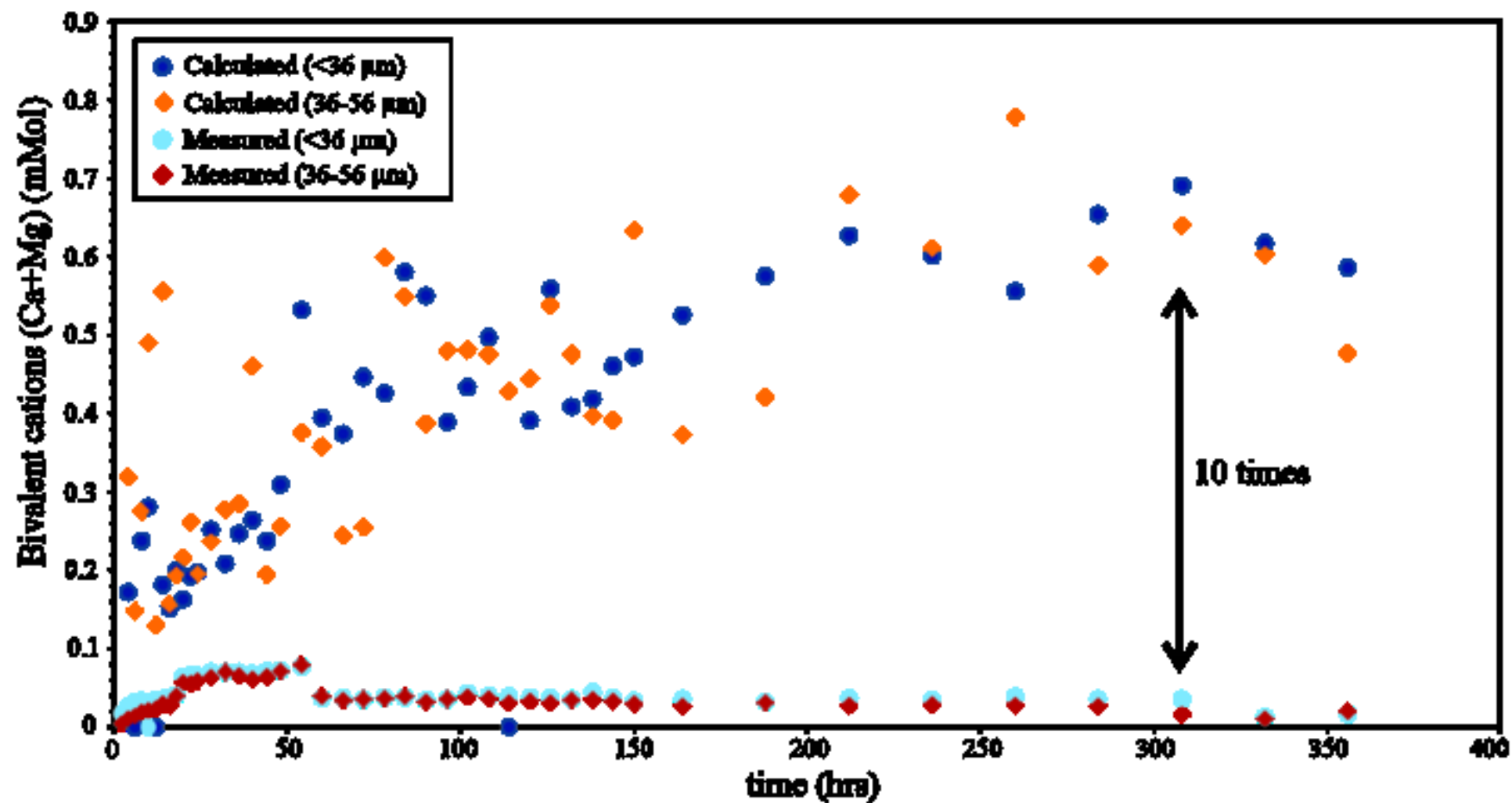
Click here to access/download
Supplementary Material
Supplementary.pdf